Accepted Manuscript

Assessment of methodologies for the solution of the Ffowcs Williams and Hawkings equation using LES of incompressible single-phase flow around a finite-size square cylinder

M. Cianferra, S. Ianniello, V. Armenio

PII: S0022-460X(19)30200-7

DOI: https://doi.org/10.1016/j.jsv.2019.04.001

Reference: YJSVI 14700

To appear in: *Journal of Sound and Vibration*

Received Date: 10 July 2018

Revised Date: 22 March 2019

Accepted Date: 1 April 2019

Please cite this article as: M. Cianferra, S. Ianniello, V. Armenio, Assessment of methodologies for the solution of the Ffowcs Williams and Hawkings equation using LES of incompressible single-phase flow around a finite-size square cylinder, *Journal of Sound and Vibration* (2019), doi: https://doi.org/10.1016/j.jsv.2019.04.001.

Assessment of methodologies for the solution of the Ffowcs Williams and Hawkings equation using LES of incompressible single-phase flow around a finite-size square cylinder

M. Cianferra[†], S. Ianniello[‡], V. Armenio[†]

[†] *University of Trieste, Dipartimento di Ingegneria e Architettura, Trieste, Italy*
[‡] *CNR-INM, Institute of Marine Engineering, Rome, Italy*

Abstract

The acoustic analogy represents a powerful tool for the prediction of noise generated by the interaction between the flow and a moving body. It is based on decoupling the acoustic problem from the fluid dynamic one: the velocity and pressure fields, obtained through a separate numerical simulation, are used as source terms in an inhomogeneous wave equation whose solution reconstructs the noise in the far field. When the method is based on the fundamental Ffowcs Williams and Hawkings (FW-H) equation, different solving methodologies may be adopted.

The present work considers the original FW-H equation and gives the advective formulation of the volume integral terms. The results are compared with those obtained with the Curle and porous formulations.

To account for volume integrals, the assumption of compact noise source is needed. This assumption is common in literature, however, in the present work, a dimensional analysis is proposed, in order to indicate in a rigorous way the cases in which the compressibility delays can be avoided. The dimensional analysis is tested in the case of an acoustic monopole field. Successively, the FW-H porous formulation is compared with the original FW-H equation in the case of an irrotational advected vortex. This example puts in evidence the different response of the two methods in the case of a vortex crossing the acoustic domain.

Then, different solution strategies of the FW-H are evaluated using a fluid dynamic dataset obtained through large eddy simulation of a turbulent flow around a finite-length cylinder with square section. The analysis allows to point out the strengths and drawback of the different techniques and to achieve, through the comparison of the different solutions, an accurate understanding of the noise source mechanisms taking place in the flow. Finally, a mixed procedure, merging the advantages of the porous formulation with the direct evaluation of the volume integral terms is proposed. It may be used in presence of significant time delays. Overall, the present study is oriented to the analysis of very low Mach number flows, although the complete porous method might be applicable in a more general framework. This aspect will require additional research in the future.

Keywords *Ffowcs Williams and Hawkings analogy, Large Eddy Simulation, hydroacoustics, square cylinder flow.*

1 Introduction

Analysis of fluid mechanic noise is of primary importance in a number of industrial and environmental applications. The acoustic pollution problems and their own impact on the environment, the stringent regulations concerning transportation industry and military applications are just few examples of the growing attention toward development of theoretical and numerical tools able to perform reliable noise predictions [1, 2]. For this reason, in the latter decades, sophisticated fluid dynamic and acoustic solvers have been developed, also due to the remarkable increase of computational resources. However, a number of aspects related to acoustic modeling need further investigation. This is especially true when noise production and propagation are related to complex physics (among the others, turbulence, shock waves or cavitation bubbles), to simultaneous presence of different bodies (with mutual interference or scattering problems) or to the presence of inhomogeneous and moving media [3, 4].

Fluid mechanic noise represents the propagation of pressure/density disturbances, therefore the evaluation of the acoustic field would require the solution of the Navier-Stokes equations (NSEs) for compressible flows. However, few studies are available in literature where the above mentioned equations are solved numerically, mostly limited to 2D cases or elementary configurations (see, for example, [5, 6]). On the other

hand, engineering applications require accounting for realistic three-dimensional (3D) geometry, often in presence of complex source systems. The direct solution of the compressible NSEs leads to fundamental problems: first, when the flow field is essentially incompressible (Mach number smaller than 0.3) the numerical algorithms suited for compressible flows are not able to produce numerical results due to the stiffness of the matrix of the coefficients of the algebraic systems of equations; second, the time scales of the fluid dynamic field are very different from those of the acoustic processes; third, the number and distribution of computational nodes should satisfy both the (fluid dynamic) need to accurately model the region close to the body surface and the (acoustic) requirement to represent the far field appropriately. These aspects make unfeasible the direct use of the Navier-Stokes equations for practical applications in acoustics. The alternative choice, well established in literature, is represented by the *acoustic analogy*, which allows to decouple the fluid dynamic problem from the acoustic one. The background idea is to treat the flow as a collection of noise sources, and to describe the way pressure signals interact and propagate in the field through the wave theory. This methodology provides a number of advantages. Starting from an essentially limited computational fluid dynamic domain, the acoustic solution can be projected into the acoustic far field at any point of interest. Moreover, due to the presence of different source terms, the inhomogeneous wave equation provides a simple identification of the dominant source mechanisms taking place in the flow. Finally, in a wide class of problems in the incompressible regime (among the others in ship hydrodynamics), the fluid dynamic field can be generated using the incompressible form of the NSEs, whereas the acoustic analogy is used to project the hydrodynamic noise in the far field.

Among the number of literature acoustic analogies, the original Lighthill analogy [7] represents a rearrangement of the fundamental conservation laws of mass and momentum into an inhomogeneous wave equation. Lighthill's work was first extended by Curle [8], who accounted for the possible presence of a body in the flow field, and subsequently by Ffowcs Williams and Hawkings [9], who developed a more comprehensive formulation in which the body could be considered in motion. Accordingly, earlier formulations appear to be special cases of the Ffowcs Williams and Hawkings (FW-H) equation. A very useful feature of the FW-H equation is that its original differential form can be turned into an integral formulation (by the use of the free-space Green's function), thus enabling the assessment of the acoustic field through a relatively simple post-processing of fluid dynamic data. Another important feature is the relationship between the acoustic pressure and three different source terms, which are representative of all possible noise-generation mechanisms. Two of these terms are in the form of surface integrals (hereafter referred to as 2D). When the integration domain corresponds to the surface of the body source, they identify two processes, namely the noise generated by the fluid displaced by the body in motion (thickness component) and that coming from the fluid dynamic pressure acting on the body surface (loading component), respectively. In this case, the 2D integrals are recognized as the "linear" terms of the FW-H equation and, for a stationary body, coincide with the former formulation proposed by Curle. The other term of the FW-H equation accounts for all possible sources occurring in the field as a result of the flow–body interaction (turbulence, vorticity, etc.); it is known as the nonlinear (quadrupole) noise and, in principle, requires a volume integration (hereafter referred to as 3D) over the whole fluid region affected by the body motion. The direct evaluation of such nonlinear term has been carried out rarely in literature, for different reasons. First of all, it has always been considered computationally demanding and complex to be implemented, due to the presence of volume integrals. Further, for many years the quadrupole noise was supposed to be significant only for bodies moving at a high speed (transonic or supersonic regime), when the flow is characterized by the presence of shock waves; in these conditions, complex generating noise mechanisms arise (depending on body motion and the position of the measurement point [10]) and all the kernels of the acoustic integrals become singular. However, it is worth pointing out that in hydrodynamics (for example for a marine propeller), the need to compute the FW-H quadrupole term in the incompressible flow regime has been recently reconsidered and its contribution to the (hydro)acoustic far field appears significant [14]. For the above mentioned reasons, alternative approaches to deal with the nonlinear term were explored, among the others the *porous formulation* [12, 13].

The porous formulation consists of moving the 2D integrals from the body surface over an external, closed and permeable surface S_P, which should contain the solid body and an appropriate fluid region. This allows to account for the contribution of the quadrupole sources, located inside the fluid region wrapped by the surface S_P, through a simple and fast 2D integration. The main drawback of the

method is that the reliability of noise prediction is sensitive to the choice of the integration domain and to the accuracy of fluid dynamic data available on S_P. Moreover, in many practical problems (as a marine propeller, or, in general, those characterized by the presence of a long, vortical wake advected downstream) the noise sources can be hardly embedded within a closed domain, and the vorticity crossing the porous surface gives rise to a spurious contribution of numerical nature. In literature, this undesired behavior is known as the *end–cap problem*.

To avoid this problem, it is common to place the porous domain in a region where the vorticity of the flow results negligible. In the case of a vorticity wake persisting downstream, the "outlet" side of the porous domain is omitted, so as to have an open domain of integration (see for example [15]).

In recent years, the porous formulation has been employed by several authors and improved in many aspects. Concerning the end–cap problem, Lockard and Casper [16] developed a correction to account for fluid dynamic sources propagating through the permeable surface. Their quadrupole boundary correction worked encouragingly for several two–dimensional test cases and was also employed for a flow around a three–dimensional cylinder. In order to reduce the spurious noise due to the end–cap problem, Rahier *et al.* [18] proposed to add 2D flux terms representing an approximation of the complementary volume integral. The effectiveness of their method was tested for an isolated vortex and a turbulent jet. Nitzorski and Mahesh [19] developed a sophisticated end–cap solving technique, based on multiple exit planes, over which the flux of quadrupole terms are subtracted and correlated to correction parameters computed dynamically; this technique was first validated considering a convecting potential vortex and, then, successfully applied to the study of the noise propagating from the turbulent flow around an infinite circular cylinder, for different Reynolds numbers.

To summarize, recent literature has demonstrated the importance of the non-linear quadrupole terms in the far field noise propagation for a wide class of engineering problems; the direct integration of the 3D volume terms has been avoided for a number of problems, the most important being the evaluation of the time-delay which makes the computation impractical. The evaluation of these terms has been reconsidered through a porous formulation which moves the surface of integration of the 2D integrals, from the body surface to a porous surface far from the body and embedding the noise source. Techniques have been developed to solve the end-cap problem related to the spurious noise generated when vorticity passes through the porous surface.

As regards the base fluid-dynamic field to be used within the context of the hybrid methods, in literature it has been well recognized that the quality of the data plays a very important role (for a discussion see the review paper of [20]). More recently, Lockard and Casper [16] found discrepancies between calculations using detached–eddy simulation (DES) and Reynolds Averaged Navier-Stokes (RANS) equations in conjunction with the Spalart-Allmaras turbulence model, thus emphasizing the need for very accurate input dataset. A similar conclusion can be found in the work of Ianniello *et al.* [17], where the authors studied the hydroacoustic behavior of a marine propeller combining a RANS simulation with the FW-H porous method; they highlighted the importance of the FW-H nonlinear terms and demonstrated the inadequacy of a RANS approach to capture the nonlinear noise sources required to achieve an accurate noise prediction. Nitzorski and Mahesh [19] underlined that for highly turbulent flows a large-Eddy Simulation (LES) led to better results than Unsteady-RANS.

The adequacy of results from LES in conjunction with acoustic analogies was investigated by different authors [21, 22], who focused on the high frequencies cut-off related to the unresolved sub-grid scales; their main conclusion was that filtering removes the small-scales fluctuations contributing to the higher derivatives of the Lighthill's tensor. However, the small scales, being not strongly correlated, are not expected to contribute significantly to the noise in the far field.

The aim of this work is to assess the different solving formulations of the FW-H equation illustrated above (namely linear-Curle, porous and direct integration of the volume term) in an archetypal case where the flow field is in the incompressible regime, and a turbulent wake develops downstream a body.

First we re-formulate the non-linear term in the advective form, necessary to deal with *wind tunnel* problems. Note that in literature the advective form of the FW-H equation was formulated for the linear terms only in Najafi-Yazdi *et al.* [25].

Second, we consider two basic configurations for validation purposes: the monopole and the advected irrotational vortex. The monopole allows to check the correctness of the implementation of the terms composing the FW-H equation considering both the porous formulation and the direct volume integration;

furthermore, the monopole is particularly suited for a significant discussion on the importance of the time delays for the computation of the volume terms. The advected irrotational vortex, also discussed in [19] to validated a specific solving approach for the end-cap problem, is here used to test the two methodologies (namely porous and direct volume integration) in case of a vortex crossing the acoustic domain.

Third, to deal with a fluid-dynamic problem, we consider a finite-size cylinder with square section, as a body source. The inlet uniform flow around the body generates vorticity and turbulence advected downstream and the wake assumes an oscillatory pattern. As well known, the flow around an elementary geometry such as a cylinder, has always represented a benchmark for CFD simulations, especially for the periodic vortex shedding mechanism occurring in a wide range of Reynolds numbers. This mechanism is responsible of a strong tonal (named aeolian) noise and different authors adopted the Curle's (linear) formulation to analyze the flow-induced noise (see, for example, [24, 23]). Even in case of such a simple configuration, we show the relevance of the non linear contribution coming from the turbulent wake, which can influence the resulting acoustic field significantly.

The body has a finite size in the spanwise direction in order to consider a realistic configuration. The finite size produces tip vortices interacting with the vorticity field generated by the cross-stream section, making the problem different from its simplified two-dimensional counterpart. The Reynolds number is large enough to generate a fully turbulent wake, characterized by a wide energetic spectrum. However, the use of a high aspect ratio enables the comparison with analogous fluid-dynamic solutions available in the literature at the central section of the cylinder. In order to obtain a realistic instantaneous velocity–pressure field, the fluid-dynamic simulation is carried out using wall–resolving LES (that is, a LES where the viscous sublayer developing in the near–wall region is directly resolved and the no-slip boundary condition is used). As above mentioned, in fact, the vorticity field generated in a wall-resolving LES contains the frequencies relevant for the noise generation and propagation, while the subgrid-scale contribution does not appreciably affect the pressure signals. In this sense, the results of the fluid-dynamic simulation can be considered as practically free from modeling errors, thus allowing for a clean comparison between different acoustic methodologies. Due to the lack of any experimental data or analogous acoustic simulations available in literature, the noise predictions will be directly compared with the pressure provided by the underlying LES, here considered as a reference quantity. A rationale for this choice can be found in [17] and will be given in a successive Section.

The paper is organized as follows. Section 2 provides a concise theoretical background, for both fluid dynamic (subsection 2.1) and acoustic (subsection 2.2) models; mathematical details on the derivation of the advective form of the non-linear terms of the FW-H equation are given in Appendix A. Section 3 shows the validation of the methodologies and algorithms on two simple cases, the monopole and the advected irrotational vortex; The subsection on monopole contains also a discussion on the importance of the time delays for the evaluation of the nonlinear terms. Section 4 contains the general features of the numerical setup for the analysis of the flow around the finite size cylinder; Section 5 contains analysis of the results for the fluid dynamic field (subsection 5.1) and for the acoustic signals (subsection 5.2). Concluding remarks are given in Section 6.

2 The mathematical formulations

Both fluid dynamic and acoustic models are based on the Navier-Stokes equations. In this context, it is essential to point out a fundamental feature of the hybrid methods. Decoupling fluid dynamics from the acoustic problem allows to handle the compressibility effects on noise generation and propagation. The compressible nature of propagation phenomena, in fact, is intrinsically described by the FW-H solving formulations (through the computation of "retarded" integral kernels), but it is completely unrelated to possible source mechanisms induced by a density perturbation. Then, if compressibility effects do not represent a source of sound on its own (as, for example, a shock wave or a collapsing bubble), it is possible and advantageous to use an incompressible fluid dynamic simulation to characterize the noise sources.

2.1 Fluid dynamic model

In LES, the large anisotropic and energy-carrying scales of motion are directly resolved through an unsteady and 3D simulation, whereas the more isotropic and dissipative small scales of motion are confined

in the sub-grid space. Scale separation is carried out through a filtering operation of the flow variables. As discussed in the Introduction, literature studies showed that the contribution of the subgrid scales (SGS) of motion on noise generation and propagation is negligible. The constant–density filtered Navier-Stokes equations in the incompressible regime read as:

$$\frac{\partial \bar{u}_i}{\partial x_i} = 0, \tag{1}$$

$$\frac{\partial \bar{u}_i}{\partial t} + \frac{\partial \bar{u}_i \bar{u}_j}{\partial x_j} = -\frac{1}{\rho_0}\frac{\partial \bar{p}}{\partial x_i} + \nu \frac{\partial^2 \bar{u}_i}{\partial x_j \partial x_j} - \frac{\partial \tau_{ij}^{sgs}}{\partial x_j}, \tag{2}$$

where the overbar denotes the filtering operation, u_i is the fluid velocity component in the x_i direction (with $i = 1, 2, 3$), p the hydrodynamic pressure, ρ_0 the fluid density and ν the kinematic viscosity. Here we use interchangeably u_1, u_2, u_3 or u, v, w as velocity components along the x_1, x_2, x_3 or x, y, z directions respectively. The SGS stress tensor $\tau_{ij}^{sgs} = \overline{u_i u_j} - \bar{u}_i \bar{u}_j$ represents the effect of the unresolved fluctuations on the resolved motion. It needs to be modeled and, in the present work, we use the Smagorinsky model:

$$\tau_{ij}^{sgs} - \frac{1}{3}\tau_{kk}^{sgs}\delta_{ij} = -2\nu_t \bar{S}_{ij}, \text{ in which } \bar{S}_{ij} = \frac{1}{2}\left(\frac{\partial \bar{u}_j}{\partial x_i} + \frac{\partial \bar{u}_i}{\partial x_j}\right).$$

The SGS eddy viscosity ν_t is expressed as:

$$\nu_t = (C_s \Delta)^2 \, |\bar{S}_{ij}| = (C_s \Delta)^2 \sqrt{2 \bar{S}_{ij} \bar{S}_{ij}}, \tag{3}$$

where C_s is the Smagorinsky constant and $\Delta = \sqrt[3]{\Delta_1 \Delta_2 \Delta_3}$ is the filter width, with Δ_i the grid spacing in the i-direction. The standard OpenFOAM implementation of the Smagorinsky model is $\nu_t = c_k \Delta^2 \sqrt{c_k / c_e} |\bar{S}_{ij}|$. Equating this expression with eq. (3) gives $C_s^2 = c_k \sqrt{c_k / c_e}$. We adopted the default values for the constants $c_e = 1.048$ and $c_k = 0.094$, which give $C_s = 0.167$. In general the value for C_s varies in the range $0.1 - 0.2$. The Van Driest function is used to bring to zero the eddy viscosity close to the solid walls.

2.2 Acoustic model

The FW-H equation accounts for the presence of a rigid body moving in a quiescent fluid and representing a discontinuity in the flow field. In our case, the body is at rest and the terms related to its own velocity drop out. Nevertheless, the surrounding fluid moves at a constant speed (along the x-axis) and the solving formulation has to be derived from the convective form of the FW-H equation. A clear derivation of the convective FW-H equation is reported in the paper of Najafi-Yazdi *et al.* [25]. There, the authors developed an integral solving formulation for the linear (surface) terms, validated it for a monopole (stationary and rotating) and a dipole in a moving medium. They also gave a detailed description of the "wind–tunnel" problem, where both the source and the observer are at rest. Note that in that paper (as well as in most papers focused on the use of the FW-H equation), the nonlinear volume term was not included in the solving formulation, since the authors assumed its contribution to be negligible or, in case, assessable through the porous formulation.

Here we derive the advective formulation of the volume term for the case of the wind tunnel flow, namely a general problem where a body at rest is immersed in a flow field with uniform velocity U_0. By the use of the free–space Green's function for the convective wave equation (see Blokhintsev [26]), it is possible to derive an integral form of the FW-H equation, where the acoustic pressure $\hat{p}$, at any point $\mathbf{x}$ and time t, is represented by the sum of surface ($\hat{p}_{2D}$) and volume integrals ($\hat{p}_{3D}$). Under the assumption of a fixed-in-space body and considering an uniform flow with velocity U_0 along the direction x_1, the surface terms read as [25]:

$$\begin{aligned} 4\pi \hat{p}_{2D}(\mathbf{x}, t) \;=\; & \frac{\partial}{\partial t}\int_{f=0}\left[(1 - M_0 \hat{r}_1)\frac{\rho_0 u_i \hat{n}_i}{r^*}\right]_\tau dS - U_0 \int_{f=0}\left[\frac{\rho_0 u_i \hat{n}_i \hat{r}_1^*}{r^{*2}}\right]_\tau dS \\ + \; & \frac{1}{c_0}\frac{\partial}{\partial t}\int_{f=0}\left[\frac{L_{ij}\hat{n}_j \hat{r}_i}{r^*}\right]_\tau dS + \int_{f=0}\left[\frac{L_{ij}\hat{n}_j \hat{r}_i^*}{r^{*2}}\right]_\tau dS, \end{aligned} \tag{4}$$

where $\hat{n}$ is the (outward) unit normal vector to the surface element dS and $\hat{r}$, $\hat{r}^*$ are unit radiation vectors (see Appendix A). The appearance of streamwise component $\hat{r}_1$ and $\hat{r}_1^*$ is due to the mean flow which advects the acoustic waves along the x_1 direction, while r and r^* are the modules of the radiation vectors $\mathbf{r}$ and $\mathbf{r}^*$ respectively, $M_0 = U_0/c_0$ is the inlet Mach number and c_0 is the speed of sound.

The integrals are calculated over a domain $S = \{\mathbf{x} : f(\mathbf{x}) = 0\}$ which can be chosen in a proper way. The tensor L_{ij} appearing in (4) is given by:

$$L_{ij} = [\rho_0 u_i \left(u_j + U_0 \delta_{1j} - v_j\right) + P_{ij}],$$

where $P_{ij} = \tilde{p}\delta_{ij} - \sigma_{ij}$ is the compressive stress tensor, being $\tilde{p} = p - p_0$ the pressure perturbation with respect to the reference value p_0 and σ_{ij} the viscous stress tensor and δ_{ij} the isotropic second order tensor.

The reference pressure p_0 is set equal to that of the fluid dynamic simulation, namely $p_0 = 0$ coming from the outlet boundary condition reported in section 4.

The volume integrals assume the form

$$\begin{aligned} 4\pi\hat{p}_{3D}(\mathbf{x},t) &= \frac{1}{c_0^2}\frac{\partial^2}{\partial t^2}\int_{f>0}\left\{T_{ij}\left[\frac{\hat{r}_i\hat{r}_j}{r^*}\right]\right\}_\tau dV \\ &+ \frac{1}{c_0}\frac{\partial}{\partial t}\int_{f>0}\left\{T_{ij}\left[\frac{2\hat{r}_i\hat{r}_j^*}{r^{*2}} + \frac{\hat{r}_i^*\hat{r}_j^* - R_{ij}^*}{\beta^2 r^{*2}}\right]\right\}_\tau dV \\ &+ \int_{f>0}\left\{T_{ij}\left[\frac{3\hat{r}_i^*\hat{r}_j^* - R_{ij}^*}{r^{*3}}\right]\right\}_\tau dV. \end{aligned} \tag{5}$$

Equation (5) contains two second–order tensors: R_{ij}^* (see Appendix A) and the well known Lighthill stress tensor T_{ij}, characterizing the FW-H quadrupole term. As known, under the assumption of negligible viscous effects and iso-entropic transformations for the fluid in the acoustic field (where we set $p' = c_0^2\tilde{\rho}$, with $\tilde{\rho}$ the density perturbation), the Lighthill tensor reads as:

$$T_{ij} = \rho_0 u_i u_j + \left(\tilde{p} - c_0^2\tilde{\rho}\right)\delta_{ij}.$$

The index τ in eqs. (4) and (5) denotes that the integral kernels are computed at the emission (retarded) time

$$\tau = t - r/c_0 = t - \frac{|\mathbf{x}(t) - \mathbf{y}(\tau)|}{c_0}. \tag{6}$$

τ is the instant at which the noise impulse starts at the source point $\mathbf{y}$, to reach the observer $\mathbf{x}$ at the observer time t. The difference between observer and emission time is known as compressibility delay and points out that sound propagates in the fluid at a finite speed. It is worth noting that, to the best of our knowledge, equation (5) has never been formulated in previous work.

Particular attention has to be paid to the meaning of function f, representing the integration domain. The points in space such that $f(\mathbf{x},t) = 0$ may describe a surface S coincident with the surface of the body–source or, alternatively, a closed (porous) surface S_p, acting as a radiating domain and embedding the body together with a fluid region around it. In the former case, the impermeability condition ($u_n = v_n$) and the assumption of a fixed-in-space body ($\mathbf{v} = 0$), reduce the pressure term $\hat{p}_{2D}$ to the Curle formulation

$$4\pi\hat{p}_{2D}(\mathbf{x},t) = \frac{1}{c_0}\frac{\partial}{\partial t}\int_S\left[\frac{\tilde{p}\hat{n}_i\hat{r}_i}{r^*}\right]_\tau dS + \int_S\left[\frac{\tilde{p}\hat{n}_i\hat{r}_i^*}{r^{*2}}\right]_\tau dS \tag{7}$$

Conversely, in the latter case, the domain should embed the body and all possible flow noise sources, in such a way to make the contribution of $\hat{p}_{3D}(\mathbf{x},t)$ (now to be evaluated over a volume external to S_p) equal to zero.

In the following, we deal with the numerical solution of the integral solving approaches discussed above. In particular, we first compare the Curle and porous formulations, in order to assess the relevance of the nonlinear terms and to identify the dominant source mechanisms taking place in the flow, both in proximity of the solid body and downstream of the body. Then, the results from the porous method are compared with a full and direct solution of the convective equation, including the volume integrals

appearing in (5). To be noted that, hereafter, when we refer to the porous formulation, we consider a surface which is open in the wake, in order to avoid the end-cap problem. This is the way the porous formulation is usually adopted, with the noteworthy exceptions discussed in Section 1 who developed numerical procedures to overcome the problem above mentioned.

2.3 Numerical models

Both fluid dynamic and acoustic fields are solved in the framework of the OpenFOAM®library, based on Finite Volume Methods (FVM). The integration of the incompressible NSEs is carried out using the fractional multistep pisoFOAM solver, with spatial derivatives discretized thorough second-order central differences, whereas implicit time advancement runs according to the Euler scheme [27]. The algorithm, including the SGS closure, has been massively validated at the laboratory of Industrial and Environmental Fluid Mechanics (IE-Fluids) of the University of Trieste, and details can be found in [28].

The FW-H solving formulations are implemented as a post-processing of LES data. Specifically, the acoustic model is implemented as follow: the flow data, pressure and velocity fields are collected on the body surface, a porous surface or a volume region, depending on the specific formulation adopted. When computing the integrals of equations (5) and (7), the mesh of the acoustic domain coincides with the fluid dynamic mesh. Thus, the elementary cells' surface and volume, that is dS and dV in the integral equations, are related to the structure of the fluid dynamic simulation. When using the porous formulation, the integrals of equation (4) are computed either taking advantage of surfaces already defined in the computational grid, or using an independent surface, given through a .stl file, over which the fluid dynamic data are linearly interpolated. The results were verified to be nearly identical in the two cases.

For the computation of the time derivatives of eqs. (4, 5) we tested second-order and fourth-order centered schemes, taking advantage of the dataset available from the CFD simulation. The use of 4th-order scheme did not improve the results with respect to 2nd-order formulas.

The equation are solved, by a forward–in–time integration method: at each source point of the integration domain, the emission time τ is fixed and identified by the time step of LES run, so that the corresponding observer time t is determined by the numerical model. Then, each signal is computed within its own time window and a data fitting procedure is implemented to calculate the resulting noise signal as the sum of single-source contributions. Due to the absence of body motion and the high value of sound speed, the compressibility delay $t - \tau$ here reduces to a time shift homogeneous in space, which does not affect the overlapping of elementary signals. In other words, the body together with its own wake, appear as a compact source and the calculation of the delays could be omitted, thus obtaining an instantaneous (incompressible) propagation of noise: this allows for a remarkable saving of CPU time and makes the computation of the volume (quadrupole) integrals feasible and even advantageous. This important issue is discussed in Sections 3.1,5.2.

3 Validation of the acoustic solver against analytical solutions

We first consider a monopole and successively an advected irrotational vortex.

3.1 The monopole

In this section the FW-H porous formulation is tested for the simple case of a monopole acoustic field. The aims are to validate the implementations of the acoustic solver and to quantify the dependence of the solution from the computation of the time delays. The following discussion holds for the wind-tunnel case as well. The need to emphasize the role of the time delays lies in the fact that their calculation makes the acoustic post-processing time-expensive and complex, and in the case of volume integration, even unaffordable. In fact, the procedure consists in storing all the source data (pressure and velocity fields of the fluid flow) for each emission time τ and performing a data-fitting over all the data to get the acoustic signal at the observer time t. The assumption that the source impulses propagate instantaneously would avoid the calculation of time delays. Here we show that this assumption is valid if a range of high frequencies does not contribute to the overall noise and can be filtered out.

According to the integral FW-H porous formulation, the acoustic pressure $\hat{p}$, evaluated at any point $\mathbf{x}$ and time t, is:

$$\hat{p}(\mathbf{x},t) = \int_{S_p} [\cdots]_\tau \, dS_p(\mathbf{y}) \tag{8}$$

where $\tau = t - |\mathbf{x}-\mathbf{y}|/c_0$ [we omit the dependence of $\mathbf{x}$ and $\mathbf{y}$ from t and τ respectively because we analyze the case in which the distance source-observer $r = |\mathbf{x}-\mathbf{y}|$ is constant in time].

S_p is the porous surface, where the noise sources are collected.

A monopole is a pressure field generated by a pulsating sphere. The pressure field is constant in the radial direction and may be represented by harmonic waves of angular frequency $\omega = 2\pi f$ traveling outward from the origin (starting at time $t_0 = 0$):

$$p(r,t) = \frac{i\rho_0 c_0 k Q}{4\pi r} e^{-i(\omega t - kr)}, \tag{9}$$

where $Q = p_I 4\pi/\rho_0 c_0 k$ is defined as *strength of an omnidirectional (monopole) source* situated at the origin, being p_I the sound pressure amplitude. We consider the real part of eq. (9) obtaining a sine wave. The radial particle velocity $u_r(r,t)$ in a spherically radiating sound field is given by Euler's equation as

$$u_r(r,t) = -\frac{1}{\rho_0} \int \frac{\partial p(r,t)}{\partial r} dt. \tag{10}$$

The porous domain S_p here considered is a sphere of radius R, discretized using 300×150 points in the angular directions ϕ and θ respectively. The outward normal to the sphere surface is given by the standard spherical coordinates

$$\begin{aligned} \hat{n}_x &= \sin(\varphi)\cos(\theta) \\ \hat{n}_y &= \sin(\varphi)\sin(\theta) \\ \hat{n}_z &= \cos(\varphi) \end{aligned}$$

with $\varphi \in [0,\pi]$ and $\theta \in [0,2\pi)$. The monopole field (eq. 9) is evaluated over the porous surface S_p in order to provide source field data. The same equation offers an analytical solution which is here evaluated at point $\mathbf{x}_{mic} = (100,0,0)$ m as a reference pressure. Due to the spherical symmetry of the problem, every point of the space at a certain distance from the origin, is equivalent.

First a wave frequency equal to $f = 1$ Hz is considered; data (p and u_r) over a sphere of radius $R = 0.1$ m are collected with a time step $dt = 0.01$s along a period $T = 600 \times dt$ s. The porous formulation is considered both accounting for the time delays (referred to as $Por\_delayON$) and without computing them (referred to as $Por\_delayOFF$). Figure 1 shows a clear overlap of the two reconstructed signals with the analytical solution, proving the correct implementation of the present porous formulation.

As regards the analysis of the time delays, the agreement between $Por\_delayON$ and $Por\_delayOFF$ was expected. In the general case we can say that the computation of the time delays is needed only when the following maximum frequency parameter satisfies

$$MFP = \frac{1}{\Delta_{del}\, f_{max}} < 1 \tag{11}$$

Being

$$\Delta_{del} = \frac{\max\limits_{\mathbf{y}\in S_p} |\mathbf{y}-\mathbf{x}_{mic}| - \min\limits_{\mathbf{y}\in S_p} |\mathbf{y}-\mathbf{x}_{mic}|}{c_0}, \tag{12}$$

and f_{max} the highest frequency at which the fluid dynamic phenomena is observed. Note that if dt is the time step at which the fluid dynamic data are stored, frequency higher than $1/dt$ are filtered out from the numerical solution.

Thus, by omitting the time delays computation, only the frequencies higher than $1/\Delta_{del}$ are erroneously reproduced.

In the present case of a spherical porous domain, $\Delta_{del} = 2R/c_0$ for any point $\mathbf{x}_{mic}$. The previous radius and time step considered (0.1 m and 0.01 s respectively) do not satisfy $MFP < 1$, thus the time delays

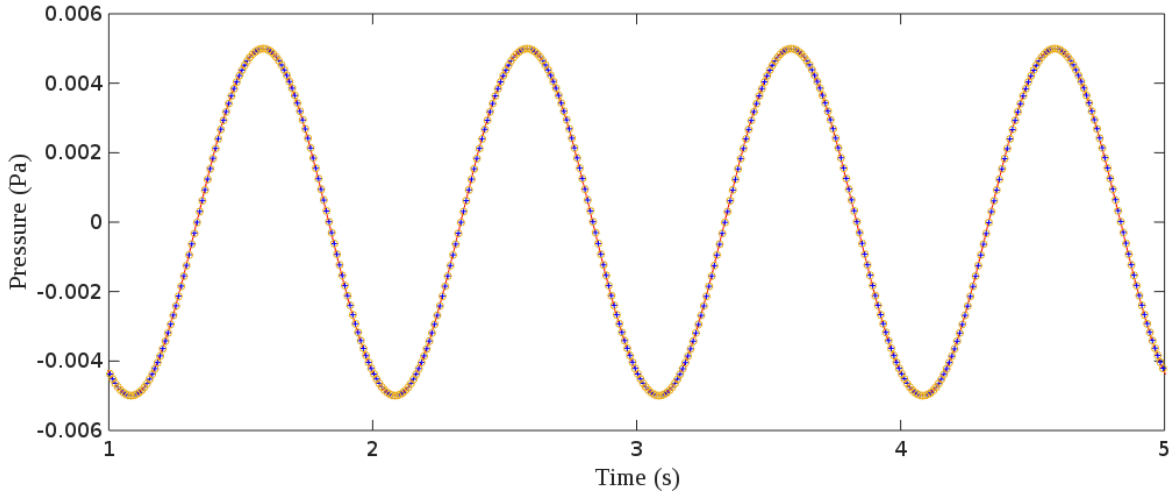

Figure 1: Comparison of a monopole pressure field p_{ref} with time solution of FW-H porous formulation, in case of time delays computation activated $Por\_delayON$ and deactivated $Por\_delayOFF$. The spherical porous domain has radius $R = 0.1$ m. p_{ref} (——); $Por\_delayON$ (o); $Por\_delayOFF$ ($+$).

computation is unessential. In practice, the source size is small enough with respect to c_0/f. In this case, the pressure impulses radiate from the porous domain simultaneously.

Results do not change (not shown), increasing the radius of the porous domain up to $R = 1$ m; in fact, in this case $\Delta_{del} = 2R/c_0 \approx 0.0066$ s, and since $dt = 0.01$ s, we obtain $MFP = 1/(0.0066 \cdot 100) = 1.6$. The time delays, for $R = 1$ m, should be significant at frequencies $f > 1/0.0066 \approx 150$ Hz. To verify this statement we consider a pressure signal p consisting of two frequencies, a low frequency $f_l < 150$ Hz and a high frequency $f_h > 150$ Hz. A radial pressure field, combined of two angular frequencies, reads as:

$$p(r,t) = \frac{p_{I_l}}{4\pi r}\sin(\omega_l t - k_l r) + \frac{p_{I_h}}{4\pi r}\sin(\omega_h t - k_h r) \tag{13}$$

where $\omega_l = 2\pi f_l$ and $\omega_h = 2\pi f_h$, $k_l = \omega_l/c_0$ and $k_h = \omega_h/c_0$. The pressure amplitudes for the lower-frequency and the higher-frequency monopole were chosen to be respectively constant $p_{I_l} = 1$ Pa and $p_{I_h} = 0.1$ Pa.

Two different double-frequency monopoles are tested, first case is composed by $f_l = 1$ Hz and $f_h = 40$ Hz and we referred to as HF signal. The second case is composed by $f_l = 10$ Hz and $f_h = 400$ Hz, and referred to as $HHF - signal$.

For the reasoning above, in the first case, the signals $Por\_delayON$ and $Por\_delayOFF$ still overlap. In fact both frequencies, f_l and f_h, are below the threshold of 150 Hz, providing $MFP \approx 166$ and $MFP \approx 4$ respectively.

Results for the HF signal case are in Figure 2. In the second case (HHF) the signal $Por\_delayOFF$ is not able to reproduce correctly the higher frequency $f_h = 400$ Hz, as shown in Figure 3 (right panel) while the standard FW-H integration, with the complete calculation of delays ($Por\_delayON$ left panel), is in agreement with the analytical solution p_{ref}.

As a further proof, we reduce the quantity Δ_{del} by decreasing the radius of the porous domain, making the source more compact. The choice of a radius $R = 0.14$ m is adequate, in fact $\Delta_{del} = 0.2/c_0 = 0.00066$ s gives $MFP = 1/(0.00066 \cdot f_{max}) < 1$ only when $f_{max} \approx 1500$ Hz. It means that the solution of the FW-H equation without time delays, on a porous domain of this size, can provide a correct signal up to 1500 Hz. The results are in Figure 4.

As a final remark, we emphasize that the the discussion above applies for the volume integrals of the standard FW-H formulation as well, where the volume is enclosed by the porous surface.

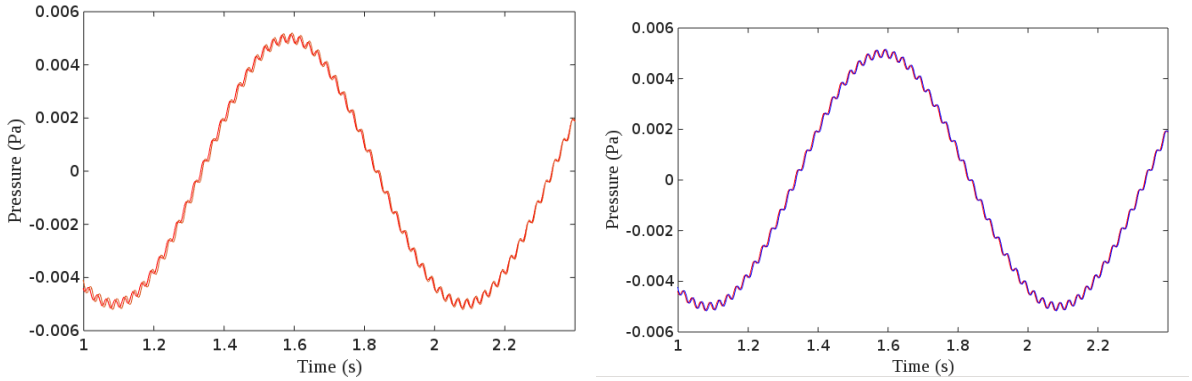

Figure 2: Comparison of a monopole pressure field p_{ref} (——) with time solution of FW-H porous formulation, in case of time delays computation activated $Por\_delayON$ (left panel, ——) and deactivated $Por\_delayOFF$ (right panel, ——). Reproduction of the HF signal. The spherical porous domain has radius $R = 1$ m. $MFP \approx 166$ for $f_l = 1$ Hz and $MFP \approx 4$ for $f_h = 40$ Hz .

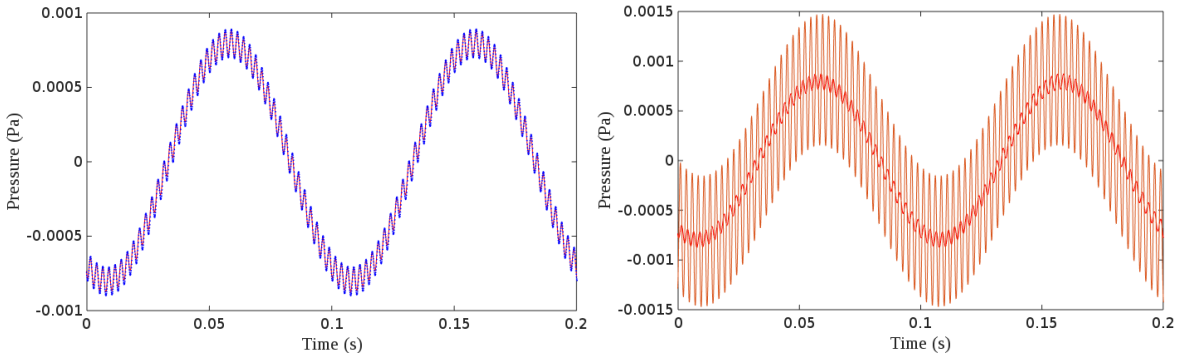

Figure 3: Comparison of a monopole pressure field p_{ref} (——) with time solution of FW-H porous formulation, in case of time delays computation activated $Por\_delayON$ (left panel, - - - -) and deactivated $Por\_delayOFF$ (right panel, ——). Reproduction of the HHF signal. The spherical porous domain has radius $R = 1$ m. $MFP \approx 16$ for $f_l = 10$ Hz and $MFP \approx 0.4$ for $f_h = 400$ Hz.

3.2 The irrotational vortex

In this section a two-dimensional potential vortex is reproduced, in order to investigate on the effect of the passage of a vortex through the boundaries of the acoustic integration domain. This test has been carried out in [19] to test the dynamic method proposed by the authors to solve the end-cap problem. Here we use this test to show that the direct integration of the volume term gives accurate results and can successfully replace the porous formulation.

The two-dimensional incompressible potential vortex is initially centered at (x_0, y_0), and is advected by a uniform and constant velocity U. The velocity potential is given by

$$\phi(x, y, t) = Ux - \frac{\Gamma\theta}{2\pi}, \tag{14}$$

where $\theta = arctg(y/x)$. The center of the vortex moves as

$$\tilde{x} = x_0 + Ut,$$
$$\tilde{y} = y_0.$$

The velocities are derived as gradients of the potential and the pressure is calculated from the nonlinear Bernoulli equation as

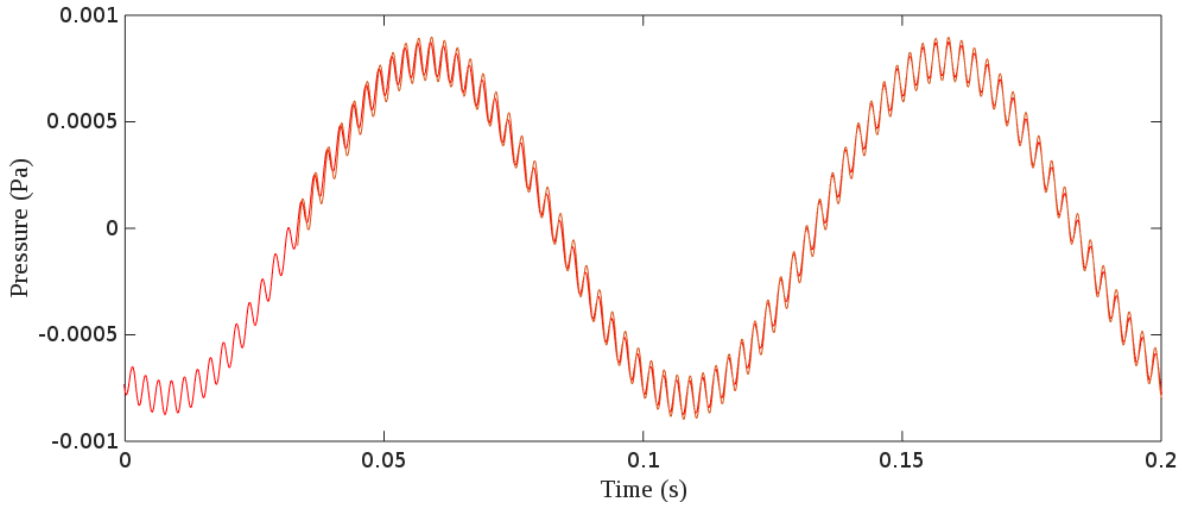

Figure 4: Comparison of a monopole pressure field p_{ref} (——) with time solution of FW-H porous formulation, in case of time delays computation deactivated $Por\_delayOFF$ (——). Reproduction of the HHF signal. The spherical porous domain has radius $R = 0.1$ m. $MFP \approx 166$ for $f_l = 10$ Hz and $MFP \approx 4$ for $f_h = 400$ Hz.

$$u(x, y, t) = U + \frac{\Gamma}{2\pi r} \sin(\theta), \tag{15}$$

$$v(x, y, t) = -\frac{\Gamma}{2\pi r} \cos(\theta), \tag{16}$$

$$p(x, y, t) = p_0 - \frac{\rho \Gamma^2}{8\pi^2 r^2}, \tag{17}$$

where r is the distance from the vortex moving center $(\tilde{x}, \tilde{y})$ and Γ is set equal to $U\pi/100$ to ensure small perturbations.

The FW-H integration domain is rectangular and two situations are considered, depicted in Figure 5: in the first case (left panel) the vortex travels inside the integration domain, so that spurious signals are not expected in this case; in the second case (right panel) the vortex center is initially positioned outside the integration domain, and moves inside the box crossing the left side of the rectangular domain.

The uniform velocity is $U = 10$ m/s and points along the x-axis. The rectangular domain is 100 m high and 200 m long and set such as $y \in [-50, 50]$ m and $x \in [0, 200]$m. The acoustic domains are discretized using 2000×1000 cells for the volume integration, and 6000 elements over the rectangular box for the porous formulation. The microphone is positioned at $(x_{mic}, y_{mic}) = (100, 51)$m, thus just one meter from

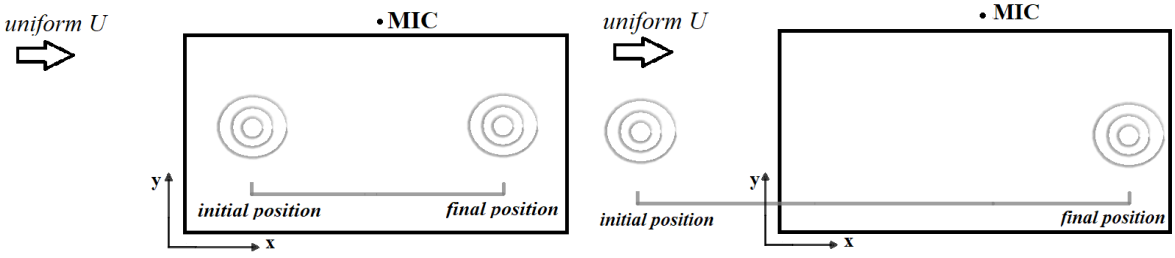

Figure 5: Sketch of the two cases reproduced: Left panel, the vortex travels inside the rectangular integration domain; right panel, the vortex starts moving outside the domain, and enters passing through the left side of the rectangular domain (referred to as *inlet side*).

the upper long side of the rectangular domain and at half length of it.

Case 1) The time step is $dt = 0.1$s and the period of the simulation is $T_1 = 10$ s. The initial position of the vortex center is $(x_0, y_0) = (50, 0)$. At the end of the period T_1 it reaches the point $(150, 0)$.

Case 2) The time step is $dt = 0.1$s and the period of the simulation is $T_2 = 20$s. The initial position of the vortex center is $(x_0, y_0) = (-50, 0)$. At the end of the period T_2 it reaches the point $(150, 0)$. Since the problem is two-dimensional, the flow field data u, v and p given in eq. (15) are collected both along the perimeter of the rectangle (which represents the porous surface) and within the area contained in the rectangle (which represents the volume region).

Direct volume integration and porous formulations are compared for the two cases. Specifically, as in [19] we compare the hydrodynamic pressure obtained through the Bernoulli equation with the pressure obtained using the FW-H equation. In the first case, the vortex never crosses the boundaries of the FW-H domain. As expected, the results are similar for both methods and compare well with the reference signal, as shown in Figure 6. The passage of the vortex gives a wavy behavior of the pressure. The minimum, at $t = 5$ s, is reached when the vortex is in correspondence of the microphone, i.e. $x_{mic} = \tilde{x}$.

In the second case, the vortex crosses the inlet side of the rectangular domain. In Figure 7, the pressure profile reconstructed by the FW-H porous formulation, at time $t = 5$ s, shows a sharp discontinuity. This spurious signal is due to the passage of the vortex through the inlet side. This behavior, also observed by [19], was eliminated by the authors using a dynamic end-cap procedure. On the other hand, Figure 7 clearly shows that the direct integration of the volume term gives a smooth behavior without the need of special treatments. The pressure signal obtained with the volume method collapses over the reference one, whereas that obtained with the porous method exhibits a slight disagreement along the entire process mindful of the sharp discontinuities undergone earlier. Both methods give the minimum pressure at time $t = 15s$, which is the time at which the vortex is in correspondence of the microphone.

An inspection of the terms composing the porous solution shows that the spurious signal is due exclusively to the integration over the inlet side. To understand this behavior, when looking at the porous equation, it is easy to recognize a term which does not have a counterpart in the volume integral formulation: it is, in short, the time-derivative of the surface integral of $\mathbf{u}_n$, where $\mathbf{u}_n$ is the velocity of the flow projected along the outward normal (unit vector) to the porous surface $\hat{n}$. In this case, the outward normal to the inlet patch is $\hat{n} = (-1, 0)$, thus the integration over this patch depends directly on the streamwise velocity u, being $\mathbf{u}_n = (-u, 0)$. The streamwise velocity at the center line ($x = \tilde{x}$) of the

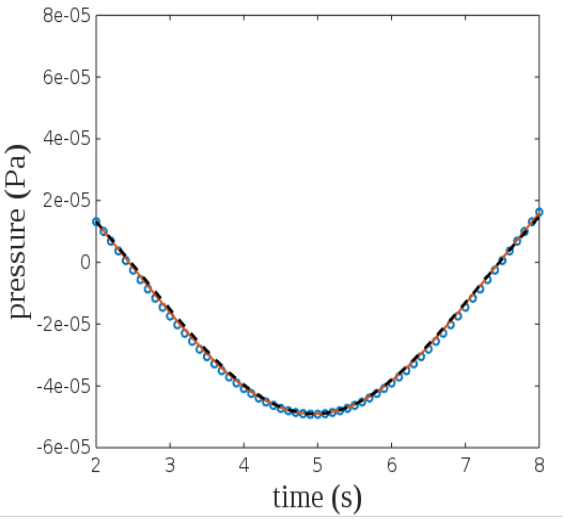

Figure 6: Comparison of FW-H direct and porous formulation for the case of an advected vortex which remains inside the integration domain, left panel of fig. 5 . Microphone positioned at (x_{mic}, y_{mic}). p_{ref} o; FW-H porous - - - -; FW-H direct ——.

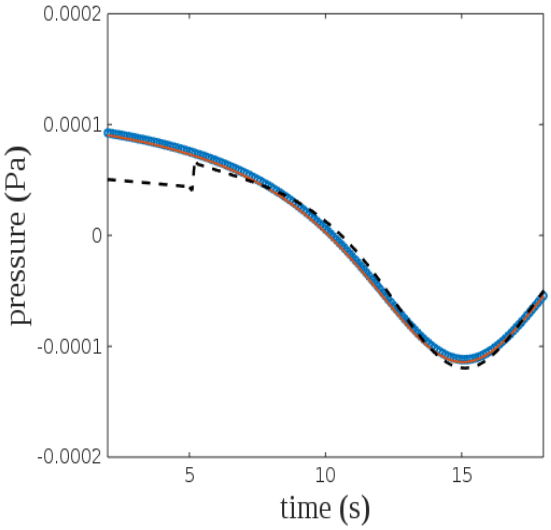

Figure 7: Comparison of FW-H direct and porous formulation for the case of an advected vortex crossing the integration domain, right panel of fig. 5 . Microphone positioned at (x_{mic}, y_{mic}). p_{ref} o; FW-H porous - - - -; FW-H direct ——.

vortex has a discontinuity. It means that, as the vortex crosses the inlet side, the term related to the velocity u contributes to the overall signal by providing a discontinuity.

4 The finite size square cylinder

Here we consider a square cylinder of side $d = 0.04$ m and length $h = 30d$. It is immersed in a uniform velocity stream $U_0 = 0.1$ m/s, so that the Reynolds number based on the side d is $Re_d = 4000$. Figure 8 shows a sketch of our test case, together with the frame of reference and geometrical parameters. The choice of a finite size cylinder has been motivated by the need to have a geometrical configuration that, in spite of its own simplicity, exhibits realistic shape. The 3D shape, in fact, allows to consider acoustic boxes closed along the lateral sides (not possible using periodic conditions) and, thus, to evaluate the acoustic solutions over closed domains, as typically happens in practical cases. Figure 9 gives a 3D view of the geometrical configuration investigated with a typical acoustic box surrounding it.

We use three different block-structured Cartesian grids, depicted in Figure 10. A first coarse grid G1 consists of about 3 millions of cells and has a slightly stretched distribution of points (for these reason it is referred to as homogeneous grid), that allows to have an acceptable resolution on the whole domain extension, but it does not solve the viscous sublayer at the body surface. This last detail is remarkable for the quality of the results as will be discussed in the next Section.

A second grid G2, of about 3 millions of cells, was designed to have a better resolution in the proximity of the cylinder. A rather accentuated stretching was employed, from the cylinder towards the boundaries of the domain, and a refinement (ref_1 in Figure 10) was applied near the cylinder surface. For grid G2, the grid spacing normal to the wall for the first layer of cells is $0.01d$ at the cylinder surface, directly resolving the viscous sublayer. As a post-processing of the turbulent data we checked that y^+ at the first grid point off the wall is in the range $0.1 - 2$, the larger value being at the corners, the mean value being around one. Overall we have roughly 6 grid points within $y^+ = 10$ around the body. The mesh G2 is stretched in the cross stream direction y, in order to have a cell expansion ratio of 30 between the first cell on the body and the last one, at the edge of the domain. The main difference between G1 and G2 is that G1 is more refined in the wake region, whereas the opposite is true for G2.

Grid G3 was obtained from the previous grid G2, considering an additional refinement in a rectangular box of size $75D \times 15D \times 50D$, referred to as ref_2 in Figure 10. Because of the refinement the grid G3 consists of 7 million of cells. In other words, G3 retains the near body resolution of G2 and the good resolution of grid G1 in the wake. This is achieved increasing by more than a factor 2 the number of cells with respect to grids G1 and G2 respectively.

As boundary conditions, the velocity is set equal to zero over the surface of the cylinder and equal to U_0 at the inlet section; then we set a symmetry condition at the planes $z = \pm 40d$ of Figure 8, a free slip condition at the planes $y = \pm 35.5d$ and a zero gradient condition at the outlet. It has to be noted that the domain is large enough to prevent from artificial reflections from the boundaries. The pressure gradient is set equal to zero at the cylinder surface and at the surfaces of the computational domain but at the outlet where we choose a reference pressure $p = 0$.

In order to keep the Courant number under 0.5, the time step was set equal to $\Delta t = 5 \times 10^{-4}$ s. Once the flow was completely developed, data were collected on a time window of about $T_{G1} = 300t_i$, $T_{G2} = 300t_i$ and $T_{G3} = 75t_i$ for the three grids respectively ($t_i = d/U_0$ being the inertial time scale), the data were sampled with a time interval $\Delta T_{G1} = (5/4)t_i$, $\Delta T_{G2} = (5/40)t_i$ and $\Delta T_{G3} = (5/40)t_i$.

The acoustic analogy was applied to determine the pressure time history at different measurement points (probes). Different open domains S_p were selected to test the capability of the porous formulation, varying their own size and shape. These domains are open both at inlet and downstream of the cylinder, thus violating the theoretical requirement for S_p to be closed. Nonetheless, as already mentioned in Section 3.2, the closure of S_p may give rise to relevant spurious noise components and the removal of the domain regions crossing the wake is rather a common practice in the application of the porous formulation (see, among the others, [29]). On the other hand, our aim here is not to deal with the mentioned end-cap problem, as rather to assess the reliability and accuracy of different FW-H-based numerical approaches. We show the results relative to two different rectangular acoustic domains: B1 and B2, the dimension being respectively $100D \times 13D \times 65D$ and $100D \times 40D \times 65D$.

Table 1: Coordinates of probes at $z = 0$ (in terms of the side d of the square section), shown in Figure 11.

	M1	M2	M3	M4
x	0	30d	0	30d
y	7d	7d	21d	21d

According to the discussion of Section 3.1, we can omit the computation of time delays. In fact, considering the largest acoustic domain B2, the maximum extension, between opposite corners, is about 5 m. The highest frequency observed is about 20 Hz. Since $\Delta_{del} = 5/1400 \simeq 0.0035$, we have $MFP = 1/(0.0035 \cdot 20) > 1$; the maximum frequency we can reproduce without the need to calculate the time delays, corresponding to $MPF = 1$, is 285 Hz. In the discussion, we considered the worst case in which the microphone is in a position that makes Δ_{del} to be equal to the maximum extension of the domain. Thus, the argument applies for every microphone location herein considered.

Note that the standard porous formulation assumes that the noise source is entirely contained within the box delimited by the porous surface S_p, but such an assumption cannot be fulfilled *a priori*. In case the porous surface does not encompasses the whole noise source, the external part has to be calculated, using for example direct volume integration. This is an additional method we test, which complements the standard porous formulation and will be adopted at the end of Section 5.2, by naming it *complete porous* approach.

For this purpose, we consider a pyramidal porous domain, adding to the surface integrals a volume integration relative to the volume region external to the pyramid. Further details on this procedure are presented in the last Section. Figure 11 shows a side view of the aforementioned acoustic domains, used for calculations.

The direct calculation of the volume terms of the FW-H equation was performed over the volume enclosed by the corresponding porous domains B1 and B2. The noise predictions were carried out at four different probes, located in the plane $z = 0$ and always selecting the y coordinate in order to set the distance of the probe from the permeable domain S_p to one diameter (see Figure 11). For completeness, the coordinates of these measurement points are listed in Table 1.

By positioning the probes within the fluid dynamic computational domain, it was possible to compare the pressure coming from the acoustic model with that provided by the LES (incompressible) solver, the effects of compressibility delays on the resulting signature being negligible. This comparison is similar to that performed with the irrotational vortex in the previous Section and by Nitzorski and Mahesh [19]. One may argue on the fact that acoustic pressure differs from the hydrodynamic one and, thus, in principle the comparison is off-based. However, this is not true for a number of reasons: first the kind of acoustic field discussed in the present paper comes solely from hydrodynamic interaction between a current and a body fixed in space. Second, the pressure signal to compare with, is just outside the volume (or porous surface) of integration, and thus acoustic and hydrodynamic pressures are very close to each other (see [17]). Finally, the FW-H equation is a way to re-write the NSEs, in the form of a wave equation. The comparisons between pressures obtained using NSEs from one side and different techniques of solution of the FW-H equation by the other side states the capability of the methodologies in reproducing a signal, which, in principle, should be exactly the same. The MFP evaluated above refers to water, so our computations refer to hydroacoustics: the fluid density was set to 1000 $\mathrm{Kg/m^3}$, while the speed of sound is equal to 1400 m/s. Note that the following discussion is valid also in air, provided that the condition $MFP > 1$ is met.

5 The hydroacoustic field around the cylinder

Hereafter, we present turbulent statistics obtained using the LES and the noise predictions provided by the different formulations solving the convective FW-H equation (Curle, porous, direct and complete porous).

5.1 The fluid dynamic field

Although interesting and meaningful for acoustic calculations, our geometry has been studied rarely and, to the best of authors knowledge, in a two–dimensional configuration only (see, for example, the experiments of Kim *et al.* [30] , Oudheusden *et al.* [31] and Lyn *et al.* [32]).

A turbulent flow around a finite-size cylinder with a square section does not exhibit any direction of homogeneity; nevertheless, due to the selected aspect ratio of the body, the behavior of the flow is comparable to the benchmark case of a 2D square section, at least in the central sections of the cylinder (around $z = 0$). This suggests to calculate the statistics averaging over longitudinal $x - y$ planes along the spanwise direction z, within a limited space interval far from the edges of the body. We make it in the range $-5d \leq z \leq 5d$.

The simulation on grid G1 exhibits a slightly larger period of vortex release when compared to the other cases, quantified by a smaller value of the Strouhal number $St = fd/U_0$. This quantity is computed from the power spectrum of the lift force coefficient. Grid G2 and G3 cases predict a Strouhal number of 0.132 and 0.136 respectively, in good agreement with data of Okajima [33]. Specifically, the authors found a constant Strouhal number of 0.133 for a square section placed in a uniform flow, with 0.5% of free stream turbulence, within the range of Reynolds numbers $1000 < Re_d < 20000$. Also, Kim et al. measured $St = 0.133$ and Lyn et al. measured the Strouhal number to be 0.132 ± 0.004 for a square cylinder wake at $Re = 21400$.

The rms of the lift coefficient is very sensitive to the grid resolution. For example, Grigoriadis et al. [34] measured a value ranging within the interval $0.55 - 1.39$ depending on the grid resolution, recirculation length and the model adopted. Specifically, the value was found to increase with grid coarsening close to the body and to the extent of separation region. Our results are in good agreement with the study of Grigoriadis et al. In fact, Cl_{rms} varies from 0.83 for G2 (which under-resolves the wake), to 0.52 for G3 which properly solves the near wall region as well as the wake.

The mean values of the drag coefficient Cd obtained with G1 , G2 and G3 are respectively 1.6, 2.07 and 2.21. While the first value is well below the typical values reported in the literature, the drag coefficients obtained with grids G2 and G3 are in agreement with previous numerical and experimental results (see [34] and literature therein reported).

A comparison between the time-averaged streamlines obtained in the three simulations is in Figure 12. G1 (top panel of Figure 12) is not able to completely resolve the boundary layer on the surface of the body and predicts a reattachment point moved further downstream, at approximately $x/d = 2$; furthermore, the grid coarseness does not allow to resolve the small recirculation zones over the streamwise-oriented body surfaces. G2 (bottom left panel of Figure 12) gives flow separation at both front corners. Shallow recirculation regions are observed over the streamwise-oriented surfaces, while two large recirculation regions appear in the wake. The end of this latter separated region is at approximately $x/d = 1$. Bottom right panel of Figure 12 shows a similar behavior of the velocity field in case G3 with respect to the previous case G2, although an improvement of the vortex definition due to the additional refinement of the grid is achieved.

The contours of space-time averaged velocity components $\langle u \rangle$ and $\langle v \rangle$ are reported in Figures 13 and 14 (for G2 and G3 respectively) together with their root mean square values. The quantities are made non dimensional with the inlet freestream velocity U_0. The small asymmetries in the contour maps are probably due to the acquisition time-window asynchronous with respect to the vortex shedding cycle, in particular for the G3 case. Figures 13,14 (bottom left panel) show the presence of high fluctuations levels in the shear layers developing at the edge of the separation regions. Large values of v_{rms} instead occur on the centerline of the wake, approximately at $x/d = 1.5$, which is behind the reattachment point (Figures 13, 14, bottom right panels). The shape of the wake, as well as the spatial distribution of the rms of velocity components, appear similar for the two grids and are in qualitatively good agreement with previous studies [31].

In Figure 15 the mean velocity profiles are shown (top panels), together with velocity root mean square profiles (bottom panels). The profiles are calculated in correspondence of the cylinder and in the near wake region. The comparison among G1, G2 and G3 profiles points out the improvement obtained considering the finer grids. In particular, the grid G1 does not allow to obtain good velocity profiles over the body surface and this also reflects in the near-body wake, where the separation region is completely mismatched. Conversely, converged results are achieved with grids G2 and G3, for which the results are

almost coincident in all sections considered.

Overall, results in this section demonstrate that the cell distribution of G1 is not good enough to reproduce accurately the flow field around the cylinder. This is due to a too coarse grid over the body surface. On the contrary, grids G2 and G3 show the convergence of results, although grid G3 is more accurate since it properly solves the wake evolution in the downstream region. Consequently, the acoustic analysis is carried out using data of simulations G2 and G3.

5.2 The acoustic analysis

As a first evidence of non-linear sources occurring in the flow, the term $(\partial^2/\partial x_i \partial x_j)T_{ij}$, related to the Lighthill tensor of equation (6), and the modulus of vorticity $|\Omega|$ are illustrated in Figure 16 for grid G3. The two quantities appear well correlated, with high vorticity regions corresponding to areas of large values of the Lighthill term. Note that regions of high vorticity are characterized by very low pressure. This result suggests that the nonlinear quadrupole contribution is expected to be large in these regions.

As already said, for comparison purposes, the probes are positioned within the fluid dynamic mesh in order to use the LES pressure as a reference data, and are such that $MFP > 1$, consistent with the assumption $t = \tau$. When calculating the spectra we remove the mean value from both the LES and the FW-H pressure signals.

The pressure spectra are evaluated at microphones M1,..,M4 of Figure 11. They are shown in Figures 17, 18 for data obtained with G2 and G3, respectively. The amplitude is reported in the logarithmic unit decibels (dB). The spectrum level was calculated as $20 \times \log_{10}(FFT(p)/p_{ref})$, where FFT denotes the Fast Fourier Transform of the signal (normalized by the number of sample points) and $p_{ref} = 1\mu Pa$ is the reference pressure adopted for water sound pressure level measurements.

In Figure 17 the peak at frequency $f \simeq 3.3$Hz corresponds to the Strouhal number $St \simeq 0.132$ and represents the typical tonal noise arising when a flow passes over an elongated object. The peak is well captured by all of the three methods considered, although it is noticeable how the porous formulation overestimates the reference data in a wide range of frequencies out of the mean peak. Linear terms and direct FW-H formulation provide quite similar results, but the latter contains the contribution of the wake that the former misses. This can be noted both at high frequencies and in the very low frequency range.

In Figure 18 the first evidence is the richer spectrum provided by the better resolution on the wake for G3, compared to G2, shown in previous Figure 17. The above discussion, for the linear and direct methods, still holds. The important difference is that the porous method results much more accurate in this case, pointing out a strong sensitiveness to the grid resolution, with respect to the direct formulation, which appears more robust under variation of the grid resolution.

For both Figures 17 and 18 we may point out that the microphone M2 is immersed in a high vorticity region (see Figure 11), that is in a region where the basic assumptions of the methods are not fulfilled.

As discussed in Section 4, it may be interesting to analyze the behavior of the acoustic solution, by coupling the porous formulation and the direct approach. To this aim, we add to the 2D integrals related to a permeable pyramidal surface, the 3D integrals provided by the complementary external volume. Figure 19 depicts this particular combination: a pyramidal domain is adopted as a porous surface, while the complementary, external volume corresponds to the region enclosed by a rectangular domain (box B2 in Figure 11). Figure 20 shows the results from such a combination (direct–porous methods, labeled as *complete porous* in the caption) at probes M3 and M4, for the case G2. These results are compared with those of the porous formulation, evaluated on the pyramidal domain.

First, we observe the better results of the FW-H porous formulation provided by integrating on a pyramidal domain. In fact, the porous signal is in a better agreement with the reference pressure, compared to the case in Figure 17 (bottom panels). This may be explained by the fact that the large box B2 lies in a region where the grid, being stretched, is quite coarse and the flow field is not well reproduced. On the other hand, integrating on the pyramidal domain of Figure 11 we are able to collect the data in a region where the flow field is better resolved. However, the contribution from the complementary volume is found to slightly improve the acoustic solutions, since the main frequency peak grows by about 5 dB. This confirms that the nonlinear sources are more spread in the field than one can infer from the visual analysis of Figure 16 and the choice of a porous domain apparently embedding the whole vorticity and

turbulence field does not guarantee an accurate prediction of noise.

Here, we did not report all the tests performed in the present research. For example, we have considered an additional sampling with time step as small as $1/5$ of that used in the paper. We did not observe significant contribution to the pressure signal associated to the higher frequencies contained in the signal and the discussion above, on the effectiveness of FW-H different methods, holds.

5.3 Acoustic far field

As a final analysis, a comparison of the acoustic far-field given by the different FW-H formulations is carried out. In particular, three microphones located in the far field, outside the fluid dynamic domain are considered: $Mf_1 = (0,\, 100D,\, 0)$, $Mf_2 = (100D,\, 100D,\, 0)$ and $Mf_3 = (100D,\, 0,\, 0)$. The pressure spectra are shown in Figure 21, for two simulations: grid G2 on the left panels and grid G3 on the right panels. First, we observe the remarkable difference between the porous and both direct and linear FW-H formulations. This is particularly true for the coarser grid G2 on the left panels and for the lower frequencies in the finer case G3. Nevertheless, the mean peak at $f = 3.3$ Hz at probes Mf_1 and Mf_2, results evident for the two simulations and it is reproduced by the three formulations. Note that, the pressure signal loses its tonal characteristics on the microphone Mf_3, located on the far downstream region. This indicates how the common dipole-like behavior associated to the acoustic field propagating from a cylinder is not entirely correct, when the vorticous wake is taken into consideration as source of noise.

A second observation regards the almost coincidence of linear terms with the direct formulation, meaning that in the far-field the volume terms are decreasing faster. This result is rather consistent with previous observations of similar studies. In fact, for the case of flow around a cylinder it is common to consider only the linear part of the acoustic equation to reproduce the far field noise. However, we have seen how the vorticity field can significantly alter the acoustic spectrum, and this is especially true for hydroacoustic cases.

According to this reasoning, the effect of grid resolution on the reproduction of the acoustic signal are found important. In case G2, where the grid is quite coarse in the wake region, linear and direct methods give results nearly coincident. This is not true in case G3, where the acoustic signal of the direct method is always larger than that of the linear method. In other words, high resolution in the wake region is needed for a proper evaluation of the far-field contribution of the non-linear quadrupole terms. This is particularly true for the probes placed in the far field out of the wake zone in the range of high frequencies, more sensitive to the vorticity dynamics. For the probe placed in the far field, in the wake behind the cylinder, the linear method is not able to reproduce the amplitude on the signal even at the peak frequency, since, there, the wake has a dominant effect over the entire spectrum. This result confirms what already observed in [35].

6 Conclusions

In the present paper we assess the accuracy of different numerical methodologies to solve the FW-H equation and estimate the noise generated by a body immersed in a uniform flow. In order to consider the nonlinear contribution to the generation of noise, the convective form of the quadrupole term has been formulated. We consider the (pure linear) Curle formulation, the standard porous formulation and the direct approach, where nonlinear terms are accounted directly computing the volume integral terms.

The account of volume integrals is feasible only in the case of compact sources, thus when time delays are not important. Otherwise the storing process of all the fluid dynamic data would cost excessively in terms of RAM and CPU time. In literature it is common to find the assumption of compact noise source. In the present work, a rigorous discussion is proposed, based on a dimensional analysis involving source length, maximum frequency and speed of sound, and giving a criterion based on the value of the non-dimensional parameter MFP. The time delays analysis is validated, through the direct volume integration and the FW-H porous formulation, in the case of an acoustic monopole field.

To compare the performance of the direct integration with those of the porous method we considered the simple case of an irrotational vortex, showing that the direct integration does not suffer for the end cap problem, typical of the porous method.

The methods have been assessed considering a fluid dynamic problem in the incompressible regime. The flow around a finite size cylinder with square section, at $Re = 4000$, was considered. Although simple, this case exhibits a number of points of interest for the generation and propagation of fluid dynamic noise. First, it is characterized by the presence of a turbulent wake, combined with a vortex sheet, which gives rise to a significant contribution from the FW-H quadrupole source terms; second, it is representative of a wide class of problems of interest in engineering. The fluid-dynamic field was solved using wall-resolving LES (carried out within the OpenFOAM®platform) and validated using available literature data.

We used the multistep fractional step PISO algorithm, which is second-order accurate in time and space, with a Courant number well below the stability limit to ensure accuracy in the results.

This simulation provides both the input data for the acoustic solvers and a reference pressure to check the reliability of noise predictions because of the negligible role played by the compressibility delays. Previous literature has proved that the flow field provided by LES is accurate for acoustic purposes, since the unresolved scales do not contribute significantly to the propagated noise.

The noise due to the fluid dynamic loads occurring on body surface is relevant in a very near region close to the body itself; on the other hand, the Curle solution is inadequate to evaluate the noise signature in the proximity of a vorticous field, like the one developing at the rear of the cylinder.

The porous formulation predicts the entire pressure spectrum, although results are sensitive to the position of measurement points, as well as to the choice of the integration domain and to the grid resolution. On the contrary, the direct approach provides a noise prediction in agreement with reference data, in points where (according to the fundamental assumption on which the FW-H equation is based) the pressure is characterized by small perturbations. This methodology is easy to be implemented, fully exploits the underlying CFD solution and makes the calculations more robust with respect to variation of the radiating domain. Nevertheless, its applicability is presently limited to problems where the effects of fluid-dynamic compressibility on noise propagation can be neglected (very low Mach number).

As a final solution method we propose the complete porous, which recalls the original formulation, considering the contribution of the volume external to the porous surface. In our test, the surface considered has a pyramidal shape and it is open on the exit plane, so that it exploits the most accurate fluid dynamic solution given by the finer grid region and allows to avoid the end-cap problem. In this sense, the complete porous might be considered as a method alternative to the porous formulation where the end-cap problem is solved. The complete porous method improves the acoustic solution with respect to the standard porous formulation. Moreover, this method might be used in cases where $MFP < 1$, since it substantially reduces the number of grid cells where the volume integrals must be evaluated, accounting for the time delays.

Acknowledgments

The present study has been supported by the project 'Nave ad alta Efficienza, WP6- Realizzazione di un software dedicato per l' analisi di valutazione del rumore aero e idrodinamico (OPENCAVIFOAM)'. Financial support from the Ministero delle Infrastutture e dei Trasporti, Italy.

Appendix

In this section we report some details about the mathematical manipulation of the convective FW-H equation and, in particular, the procedure which allows to write down the integral form of the nonlinear terms (5). The convective FW-H equation may be easily obtained from the conservation laws of mass and momentum, by accounting for the presence of a medium moving at a constant velocity $\mathbf{U}_0$; then, at each point, the fluid velocity is $\mathbf{U}_0 + \mathbf{u}$, being $\mathbf{u}$ the local perturbation velocity, and the equation reads [25]

$$\Box_C^2 p'(\mathbf{x},t) = \left(\frac{\partial}{\partial t} + U_{0j}\frac{\partial}{\partial x_j}\right)[Q_k \hat{n}_k \delta(f)] - \frac{\partial}{\partial x_i}[L_{ij}\hat{n}_j\delta(f)] + \frac{\partial^2}{\partial x_i \partial x_j}[T_{ij}H(f)] \tag{18}$$

where $\delta(f)$ and $H(f)$ are the Dirac and Heaviside functions, respectively, and

$$\Box_C^2 = \left[\frac{\partial^2}{\partial t^2} - c_0^2\frac{\partial^2}{\partial x_i \partial x_j} + 2U_{0j}\frac{\partial^2}{\partial t \partial x_j} + U_{0i}U_{0j}\frac{\partial^2}{\partial x_i \partial x_j}\right]$$

represents the convective form of the D'Alembert operator. Furthermore

$$\begin{aligned} Q_k &= [\rho\,(u_k + U_{0k} - v_k) + \rho_0\,(v_k - U_{0k})] \\ L_{ij} &= [\rho u_i\,(u_j + U_{0j} - v_j) + P_{ij}] \\ T_{ij} &= \left[\rho u_i u_j + P_{ij} - c_0^2\tilde{\rho}\delta_{ij}\right] \end{aligned}$$

where P_{ij} is the compressive stress tensor, $\tilde{\rho}$ the perturbation density, c_0 the sound speed and δ_{ij} the Kronecker delta. Without loss of generality, it can be assumed that the mean flow velocity $\mathbf{U}_0$ is along the positive x_1-direction. By using the convective form of the free-space Green function

$$G(\mathbf{x},t;\mathbf{y},\tau) = \frac{\delta(g)}{4\pi r^*} \qquad \text{with} \qquad g = \tau - t + \frac{r}{c_0},$$

where $(\mathbf{x},t)$ and $(\mathbf{y},\tau)$ are the observer and source position and time, respectively, and

$$r^* = \sqrt{(x_1-y_1)^2 + \beta^2\left[(x_2-y_2)^2 + (x_3-y_3)^2\right]}; \qquad r = \frac{-M_0\,(x_1-y_1) + r^*}{\beta^2} \qquad \beta = \sqrt{1-M_0^2}; \quad (19)$$

with the components of the unit radiant vectors given by

$$\hat{r}_1^* = \frac{(x_1-y_1)}{r^*} \quad ; \quad \hat{r}_2^* = \beta^2\frac{(x_2-y_2)}{r^*} \quad ; \quad \hat{r}_3^* = \beta^2\frac{(x_3-y_3)}{r^*} \tag{20}$$

and

$$\hat{r}_1 = -\frac{M_0}{\beta^2} + \frac{1}{\beta^2}\frac{(x_1-y_1)}{r^*} \quad ; \quad \hat{r}_2 = \frac{(x_2-y_2)}{r^*} \quad ; \quad \hat{r}_3 = \frac{(x_3-y_3)}{r^*}, \tag{21}$$

equation (18) may be turned into an integral form. The first two source terms on the right–hand–side give rise to the surface integrals of equation (4) and the procedure is described in detail in [25]. An analogous transformation may be carried out on the third (quadrupole) term, which, in essence, requires the manipulation of the double spatial derivative of the Green function

$$\frac{\partial^2}{\partial x_i \partial x_j}\left[\frac{\delta(g)}{r^*}\right]$$

Starting from

$$\frac{\partial}{\partial x_i}\left[\frac{\delta(g)}{r^*}\right] = -\frac{\hat{r}_i}{c_0 r^*}\frac{\partial}{\partial t}\left[\delta(g)\right] - \frac{\hat{r}_i^*}{r^{*2}}\delta(g)$$

we have

$$\begin{aligned} \frac{\partial}{\partial x_j}\left\{\frac{\partial}{\partial x_i}\left[\frac{\delta(g)}{r^*}\right]\right\} &= \frac{\partial}{\partial x_j}\left\{-\frac{1}{c_0}\frac{\hat{r}_i}{r^*}\frac{\partial}{\partial t}\left[\delta(g)\right] - \frac{\hat{r}_i^*}{r^{*2}}\delta(g)\right\} = \\ &- \frac{1}{c_0}\frac{\partial}{\partial x_j}\left[\frac{\hat{r}_i}{r^*}\right]\cdot\left\{\frac{\partial}{\partial t}\left[\delta(g)\right]\right\} - \frac{1}{c_0}\frac{\hat{r}_i}{r^*}\cdot\left\{\frac{\partial}{\partial x_j}\left(\frac{\partial}{\partial t}\left[\delta(g)\right]\right)\right\} \\ &- \frac{\partial}{\partial x_j}\left[\frac{\hat{r}_i^*}{r^{*2}}\right]\cdot\left\{\delta(g)\right\} - \frac{\hat{r}_i^*}{r^{*2}}\cdot\left\{\frac{\partial}{\partial x_j}\left[\delta(g)\right]\right\} \end{aligned}$$

From the relations

$$\begin{aligned} \frac{\partial}{\partial x_j}\left[\frac{\hat{r}_i}{r^*}\right] &= -\frac{1}{r^*}\frac{\partial \hat{r}_i}{\partial x_j} - \frac{\hat{r}_i\hat{r}_j^*}{r^{*2}} \\ \frac{\partial}{\partial x_j}\left(\frac{\partial}{\partial t}\left[\delta(g)\right]\right) &= -\frac{\hat{r}_j}{c_0}\frac{\partial^2}{\partial t^2}\left[\delta(g)\right] \\ \frac{\partial}{\partial x_j}\left[\frac{\hat{r}_i^*}{r^{*2}}\right] &= \frac{1}{r^{*2}}\frac{\partial \hat{r}_i^*}{\partial x_j} - 2\frac{\hat{r}_i^*\hat{r}_j^*}{r^{*3}} \\ \frac{\partial}{\partial x_j}\left[\delta(g)\right] &= -\frac{\hat{r}_j}{c_0}\frac{\partial}{\partial t}\left[\delta(g)\right] \end{aligned}$$

we obtain

$$\frac{\partial^2}{\partial x_i \partial x_j}\left[\frac{\delta(g)}{r^*}\right] = +\frac{1}{c_0^2}\frac{\hat{r}_i\hat{r}_j}{r^*}\frac{\partial^2}{\partial t^2}\left[\delta(g)\right] + \frac{1}{c_0}\left[\frac{2\hat{r}_i\hat{r}_j^*}{r^{*2}} - \frac{1}{r^*}\frac{\partial \hat{r}_i}{\partial x_j}\right]\frac{\partial}{\partial t}\left[\delta(g)\right] + \left[\frac{2\hat{r}_i^*\hat{r}_j^*}{r^{*3}} - \frac{1}{r^{*2}}\frac{\partial \hat{r}_i^*}{\partial x_j}\right]\delta(g) \quad (22)$$

Concerning the spatial derivative of $\hat{r}_i^*$, we have

$$\begin{aligned}\frac{\partial \hat{r}_i^*}{\partial x_j} &= \frac{\partial}{\partial x_j}\left[\frac{r_i^*}{r^*}\right] = \frac{1}{r^*}\frac{\partial r_i^*}{\partial x_j} - \frac{r_i^*}{r^{*2}}\frac{\partial r^*}{\partial x_j} = \frac{1}{r^*}\frac{\partial r_i^*}{\partial x_j} - \frac{\hat{r}_i^*\hat{r}_j^*}{r^*} \\ &= \frac{1}{r^*}\begin{bmatrix}1 & 0 & 0\\ 0 & \beta^2 & 0\\ 0 & 0 & \beta^2\end{bmatrix} - \frac{\hat{r}_i^*\hat{r}_j^*}{r^*} = \frac{1}{r^*}\left[R_{ij}^* - \hat{r}_i^*\hat{r}_j^*\right] \end{aligned} \quad (23)$$

where we have set

$$R_{ij}^* = \begin{bmatrix}1 & 0 & 0\\ 0 & \beta^2 & 0\\ 0 & 0 & \beta^2\end{bmatrix}$$

On the other hand, by reminding (20) and (21), it is easy to see

$$\hat{r}_1 = -\frac{M_0}{\beta^2} + \frac{1}{\beta^2}\hat{r}_1^* \quad ; \quad \hat{r}_2 = \frac{1}{\beta^2}\hat{r}_2^* \quad ; \quad \hat{r}_3 = \frac{1}{\beta^2}\hat{r}_3^*$$

so that

$$\frac{\partial \hat{r}}{\partial x_j} = \frac{1}{\beta^2}\frac{\partial \hat{r}^*}{\partial x_j} = \frac{1}{\beta^2 r^*}\left[R_{ij}^* - \hat{r}_i^*\hat{r}_j^*\right]$$

Finally, equation (22) reads

$$\begin{aligned}\frac{\partial^2}{\partial x_i \partial x_j}\left[\frac{\delta(g)}{r^*}\right] &= +\frac{1}{c_0^2}\frac{\hat{r}_i\hat{r}_j}{r^*}\frac{\partial^2}{\partial t^2}\left[\delta(g)\right] \\ &+ \frac{1}{c_0}\left[\frac{2\hat{r}_i\hat{r}_j^*}{r^{*2}} + \frac{1}{\beta^2 r^{*2}}\left(\hat{r}_i^*\hat{r}_j^* - R_{ij}^*\right)\right]\frac{\partial}{\partial t}\left[\delta(g)\right] \\ &+ \left[\frac{3\hat{r}_i^*\hat{r}_j^* - R_{ij}^*}{r^{*3}}\right]\delta(g) \end{aligned} \quad (24)$$

It 's worth pointing out that under the assumption $M_0 << 1$ we have $\beta \approx 1$ and, consequently, $r = r^*$, $R_{ij}^* = \delta_{ij}$; then, equation (24) reduces to the classic form

$$\frac{\partial^2}{\partial x_i \partial x_j}\left[\frac{\delta(g)}{r}\right] = +\frac{1}{c_0^2}\frac{\hat{r}_i\hat{r}_j}{r}\frac{\partial^2}{\partial t^2}\left[\delta(g)\right] + \frac{1}{c_0}\left[\frac{3\hat{r}_i\hat{r}_j - \delta_{ij}}{r^2}\right]\frac{\partial}{\partial t}\left[\delta(g)\right] + \left[\frac{3\hat{r}_i\hat{r}_j - \delta_{ij}}{r^3}\right]\delta(g)$$

The product of equation (24) by the Lighthill tensor T_{ij} exactly gives rise to the integral kernels of equation (5).

References

[1] Carlton J. S., Vlasic D., "Ship vibration and noise: some topical aspects", *1st International Ship Noise and Vibration Conference*, 1-11, (2005).

[2] Murphy E., King E., "Environmental Noise Pollution", *Elsevier*, (2014).

[3] Wagner C. A., Huttl T., Sagaut P., "Large-Eddy Simulation for Acoustics", *Cambridge University Press*, (2007).

[4] Lele S.K., Nichols J.W., "A second golden age of aeroacoustics?", *Phil. Trans. R. Soc.*, A 372: 20130321, (2014).

[5] Inoue O. and Hatakeyama N., "Sound generation by a two-dimensional circular cylinder in a uniform flow", *Journal of Fluid Mechanics*, 471, 285-314, (2002).

[6] Marsden O., Bogey C. and Bailly C., "Direct noise computation of the turbulent flow around a zero-incidence airfoil", *AIAA Journal*, 46(4), 874-883 (2008).

[7] Lighthill M.J., "On sound generated aerodynamically. I General theory", *Proceedings of Royal Society*, A211(11079), 564, (1952).

[8] Curle N., "The influence of solid boundaries upon aerodynamic sound", *Proceedings of Royal Society* A231(1187), 505-514, (1955).

[9] Ffowcs-Williams J.E. and Hawkings D.L., "Sound generation by turbulence and surfaces in arbitrary motion", *Philosophical Transaction of Royal Society*, 264(A1151), 321-342, (1969).

[10] Ianniello S., "New perspectives in the use of the Ffowcs Williams-Hawkings equation for aeroacoustic analysis of rotating blades", *Journal of Fluid Mechanics*, 570, 79–127, (2007).

[11] Lyrintzis A. S., "Review. The use of Kirchhoff's methods in computational aeroacoustics", *ASME Journel of Fluids Engineering*, 202(4), (1997).

[12] Di Francescantonio P., "A new boundary integral formulation for the prediction of sound radiation", *Journal of Sound & Vibration*, 202(4), 491-509, (1997).

[13] K. S. Brentner and F. Farassat, "Analytical comparison of the acoustic analogy and Kirchhoff formulation for moving surfaces", *AIAA Journal*, 36 (8), 1379-1386, (1998).

[14] Ianniello S., "The Ffowcs Williams-Hawkings equation for hydroacoustic analysis of rotating blades. Part I. The rotpole", *Journal of Fluid Mechanics*, 797, 345–388, (2016).

[15] Lloyd T., Rijpkema D. and van Wijngaarden E., " Marine propeller acoustic modelling: comparing CFD results with an acoustic analogy method ", *Fourth International Symposium on Marine Propulsors*, (2015).

[16] Lockard D. P. and Casper J. H., "Permeable surface corrections for Ffowcs Williams and Hawkings integrals", *11th AIAA/CEAS Aeroacoustics Conference*, AIAA-2005-2995, (2015).

[17] Ianniello S., Muscari R. and Di Mascio A., "Ship underwater noise assessment by the acoustic analogy. Part I: nonlinear analysis of a marine propeller in a auniform flow", *Journal of Marine Science & Technology*, 18(4), 547-570, (2013).

[18] Rahier G., Huet M. and Prieur J., "Additional terms for the use of Ffowcs Williams and Hawkings surface integrals in turbulent flows", *Computers & Fluids*, 120, 158-172, (2015).

[19] Nitzorski Z. and Mahesh K., "A dynamic technique for sound computation using the Ffowcs Williams and Hawkings equations", *Physics of Fluids*, 26(11), 115101, (2014).

[20] K. S. Brentner and F. Farassat, "Modeling aerodynamically generated sound of helicopter rotors", *Progress in Aerospace Sciences* 39, 83–120 (2003).

[21] Piomelli U., Craig L. S. and Sarkar S., "On the computation of sound by large-eddy simulation", *Journal of Engineering and Mathematics* 32, 217-236, (1997).

[22] Seror C., Sagaut P., Bailly C., Juvé D., "On the radiated noise computed by large-eddy simulation", *Physics of Fluids* 13(2), (2000).

[23] Martinez-Lera P., Muller A., Schram C., Rambaud P., Desmet W., Anthoine J., "Robust aeroacoustic computations based on Curle's and Powell's analogies", *Proceedings of the International Conference on Noise and Vibration Engineering*, 513-524, (2008).

[24] Gloerfelt X., Perot F., Bailly C., Juve D., "Flow-induced cylinder noise formulated as a diffraction problem for low Mach numbers", *Journal of Sound and Vibration*, 287, 129-151, (2005).

[25] Najafi-Yazdi A., Bres G. A. and Mongeau L., "An acoustic analogy formulation for moving sources in uniformly moving media", *Proceedings of Royal Society London*, A467, 144-165, (2011).

[26] Blokhintsev D., Acoustics of a nonhomogeneous moving media, NACA TM–1399 (http://ntrs.nasa.gov), (1956).

[27] Issa R.I., "Solution of the implicitly discretised fluid flow equations by operator-splitting", J Comp Phys, Volume 62, Issue 1, Pages 40-65, (1986).

[28] Cintolesi C., Petronio A., Armenio V., "Large eddy simulation of turbulent buoyant flow in a confined cavity with conjugate heat transfer", *Physics of Fluids* 27, (2015).

[29] Bensow R.E., Liefvendhal M., "An acoustic analogy and scale-resolving flow simulation methodology for the prediction of propeller radiated noise", *31th Symposium on Naval Hydrodynamics, California,* (2016).

[30] Kim K.C., Lee M. B., Yoon S. Y., Boo J. S. Chun H. H., "Phase averaged velocity field in the near wake of a square cylinder obtained by a PIV method", *Journal of Visualization*, 5(1), 29-36, (2002).

[31] van Oudheusden B. W., Scarano F., van Hinsberg N. P., Watt W., "Phase-resolved characterization of vortex shedding in the near wake of a square-section cylinder at incidence", *Experiments in Fluids*, 39, 86-98, (2005).

[32] Lyn, D. A., Einav, S., Rodi, W. and Park, J. H., "A Laser-Doppler Velocimetry Study of the Ensemble-averaged Characteristics of the Turbulent Near Wake of a Square Cylinder", *J. Fluid Mech.*, 304, 285-319, (1995).

[33] Okajima A., "Strouhal numbers of rectangular cylinders", *Journal of Fluid Mechanics*, 123, 379-398, (1982).

[34] Grigoriadis D.G.E., Bartzis J.G. and Goulas A., "LES of the flow past a rectangular cylinder using the immersed boundary concept", *Int. J. Numer. Meth. Fluids*, 41:615–632, (2003).

[35] Ianniello S., Muscari R. and Di Mascio A., "Ship underwater noise assessment by the acoustic analogy. Part II: hydroacoustic analysis of a ship scaled model", *Journal of Marine Science & Technology*, 18(4), 547-570, (2013).

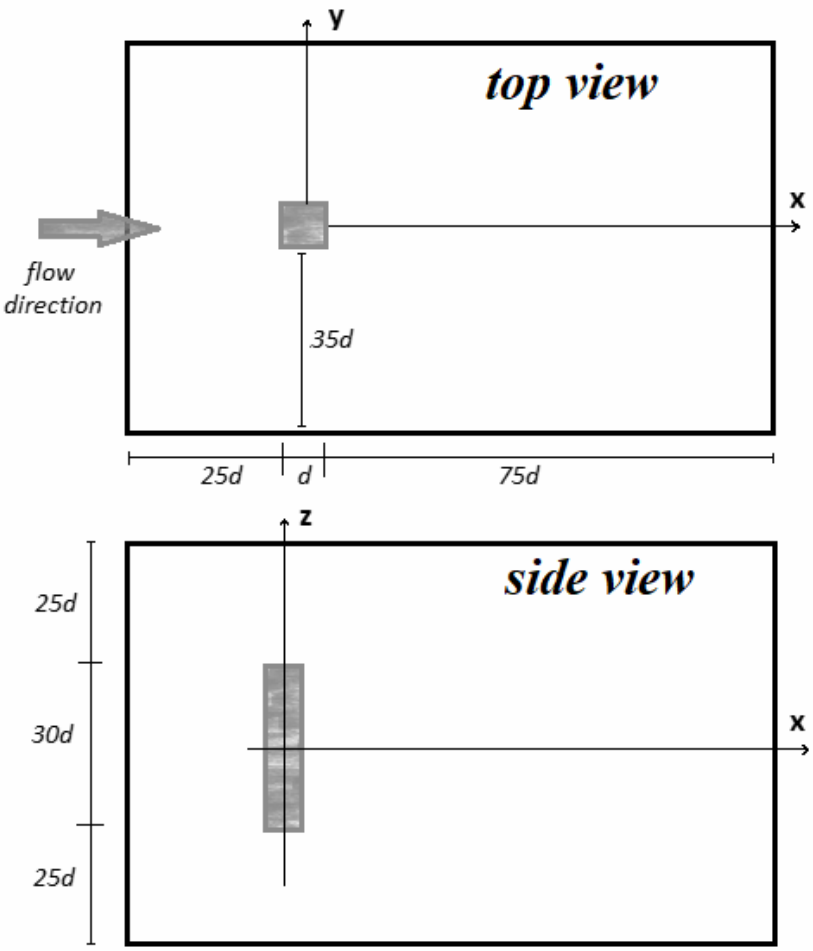

Figure 8: Computational domain for the flow past the cylinder with square section.

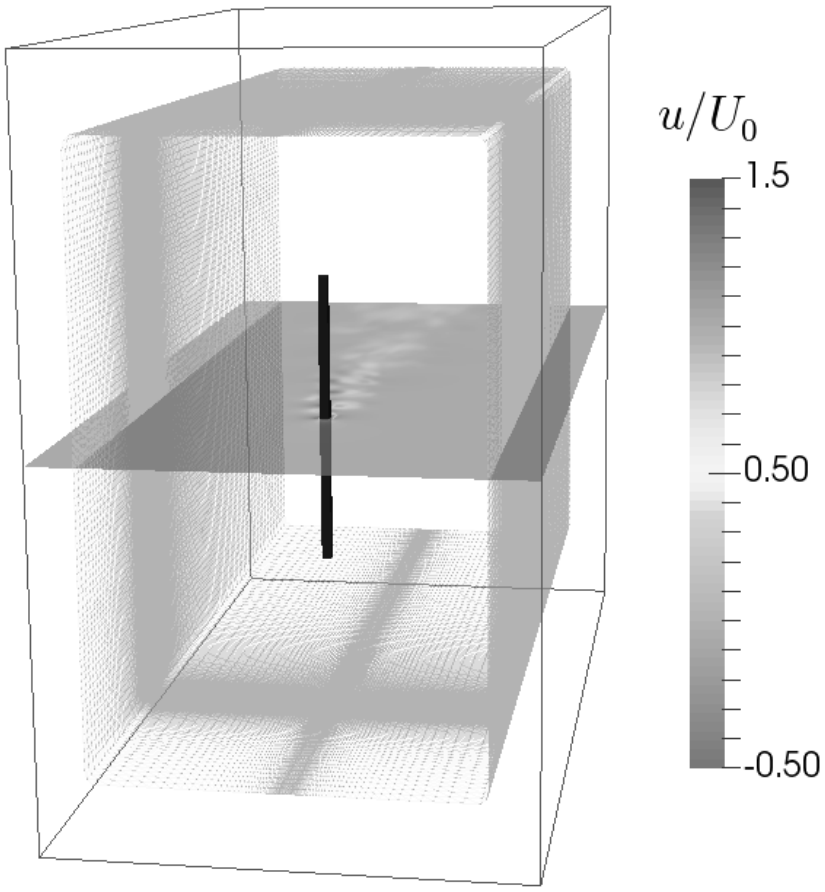

Figure 9: 3D view, computational domain around the finite-size cylinder with square section. The computational grid is the black outline, while an example of porous domain considered for the FW-H formulation is displayed in light gray.

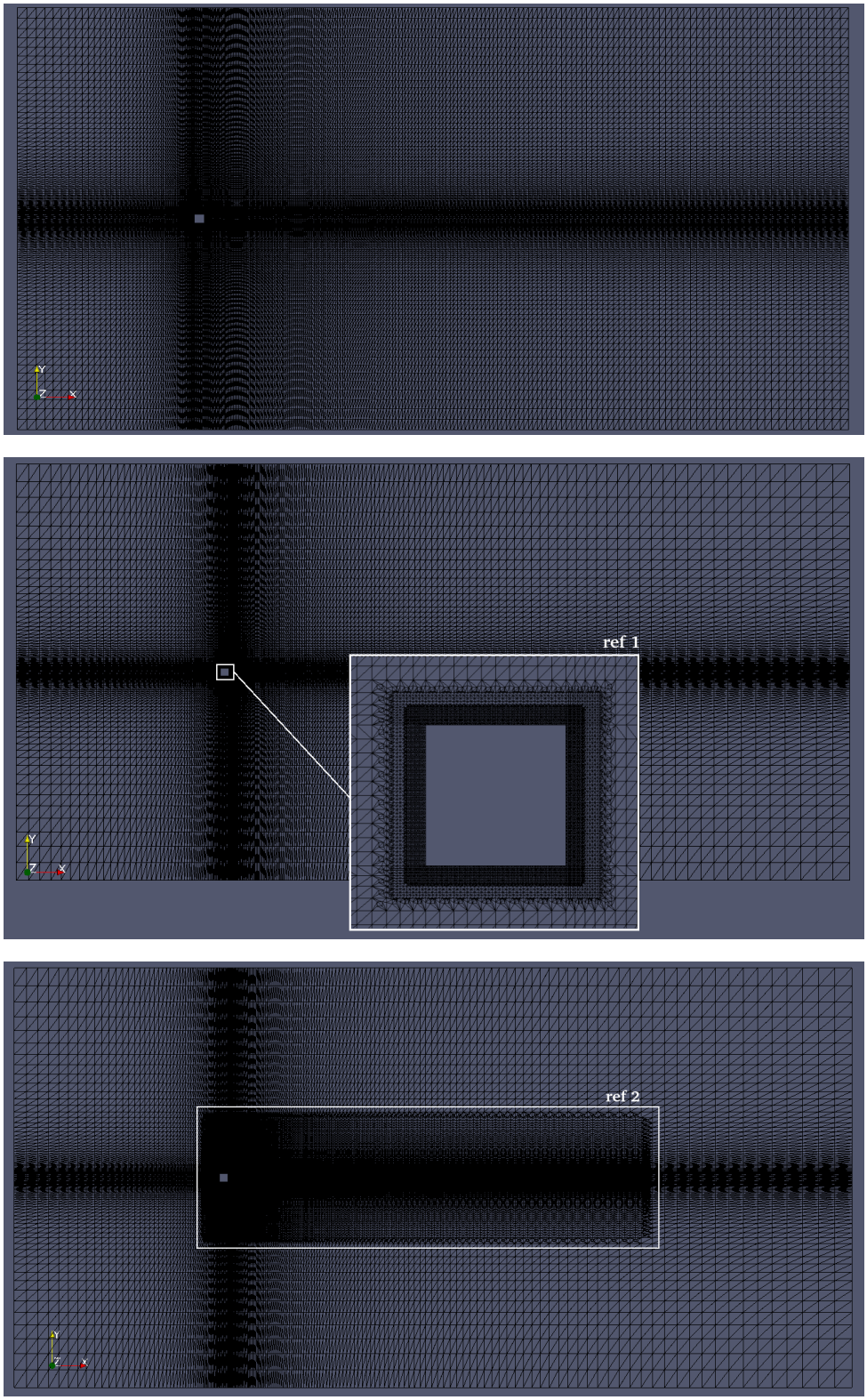

Figure 10: Computational grids adopted for the three Large-Eddy Simulations. G1 top panel; G2 mid panel; G3 bottom panel. The withe boxes point out the refinement regions ref_1 and ref_2.

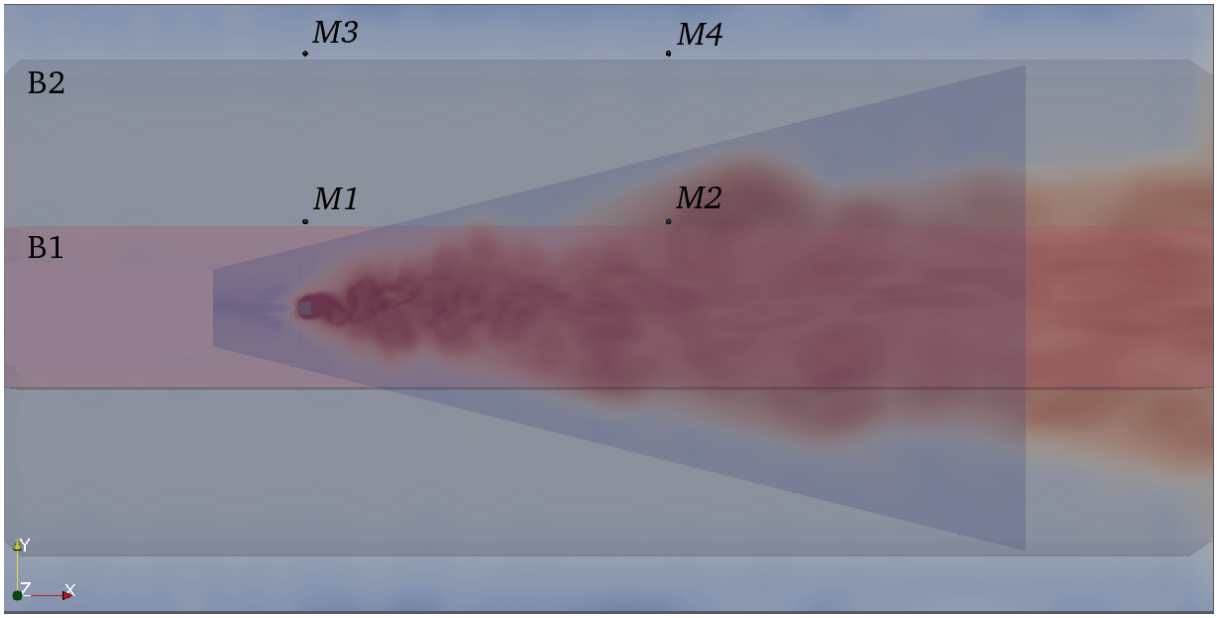

Figure 11: Two-dimensional sketch of the xy–plane ($z = 0$) and the corresponding cross–sections of different porous domains herein adopted: two concentric rectangular open boxes B1 and B2 and a pyramid. Points M1,..,M4 indicate the probes.

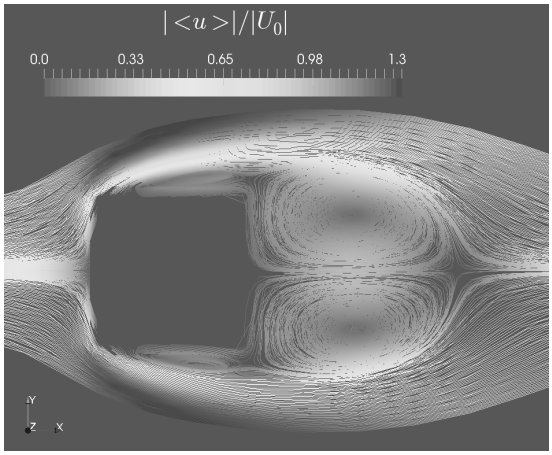

Figure 12: Mean flow streamlines together with contour map of the space-time averaged velocity magnitude made non-dimensional with U_0. Grid G1 (left panel); Grid G2 (bottom left panel); Grid G3 (bottom right panel).

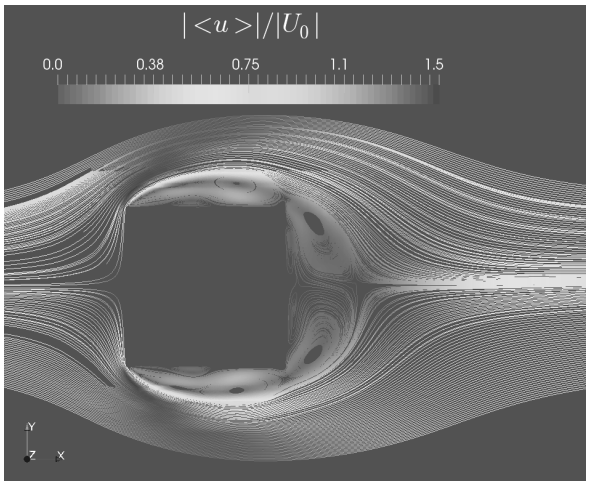

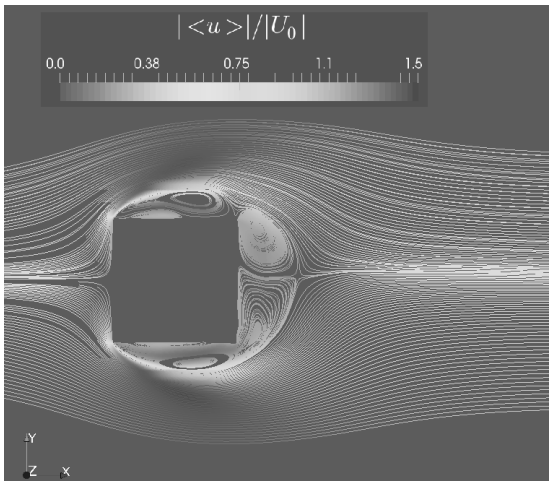

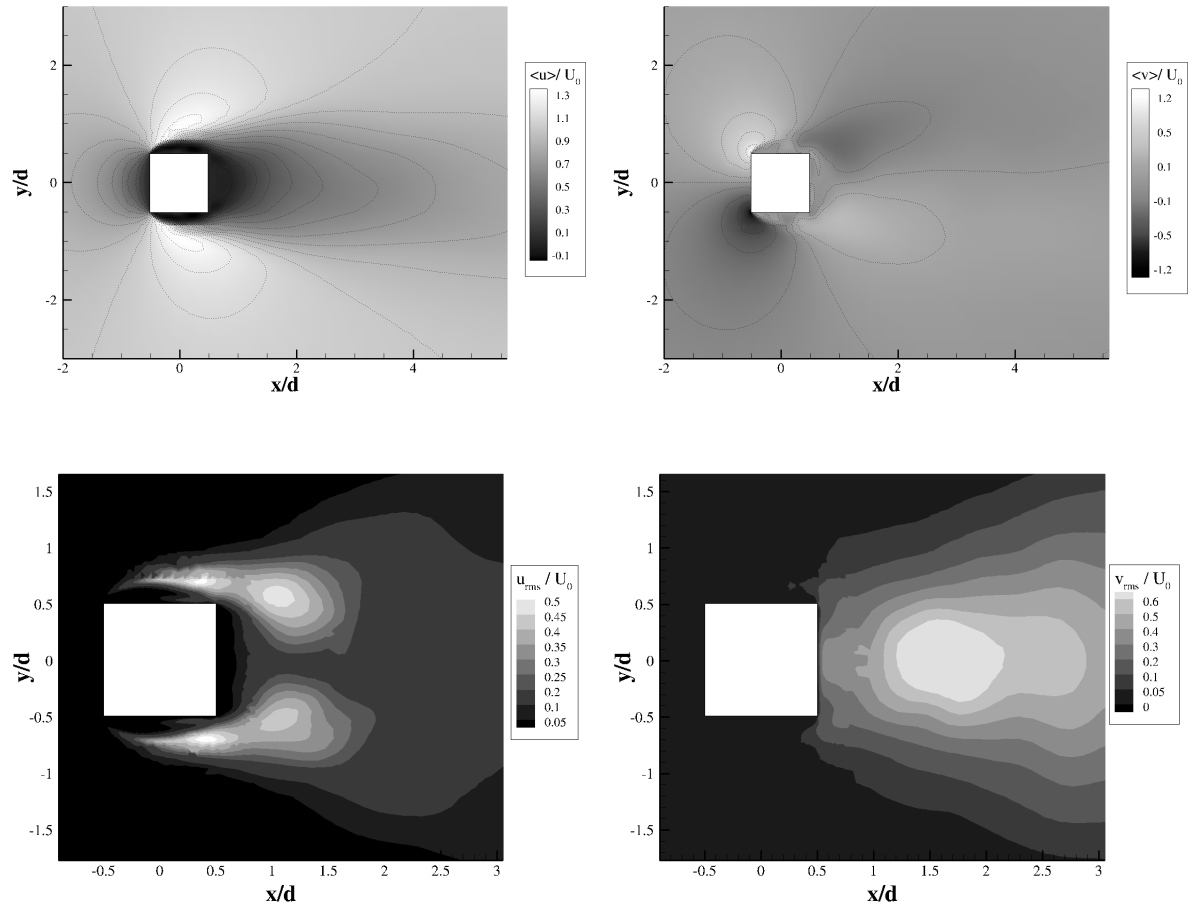

Figure 13: Contours of space-time averaged quantities: (a) $\langle u \rangle / U_0$; (b) $\langle v \rangle / U_0$; (c) u_{rms}/U_0; (d) v_{rms}/U_0. G2 grid simulation.

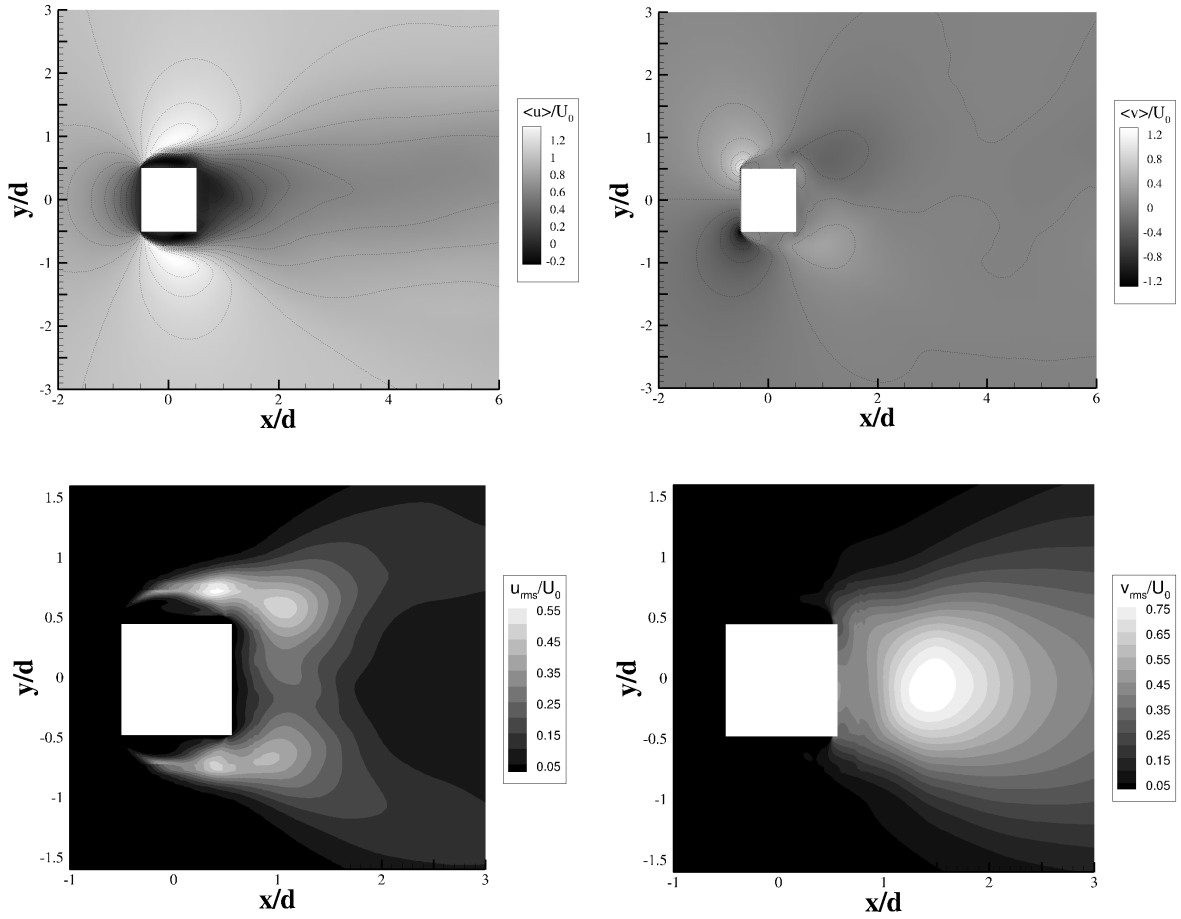

Figure 14: Contours of space-time averaged quantities: (a) $\langle u \rangle / U_0$; (b) $\langle v \rangle / U_0$; (c) u_{rms}/U_0; (d) v_{rms}/U_0. G3 grid simulation.

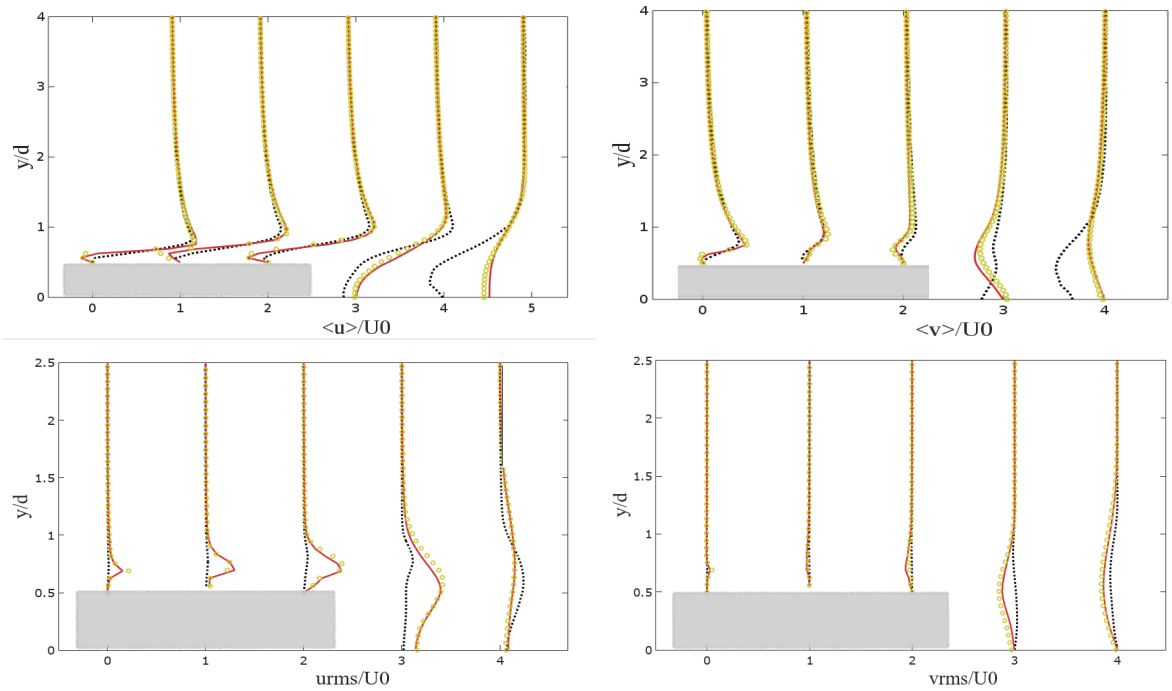

Figure 15: Space-time averaged velocity $\langle u \rangle$, $\langle v \rangle$ and u_{rms}, v_{rms} plotted along lines, at $x/d = -0.25$, 0, 0.25, 1, 2; the profiles are moved along the abscissae axis of $0, 1, 2, 3, 4$ respectively, to make the results clear. G1 (- - - -); G2 (——); G3 (○).

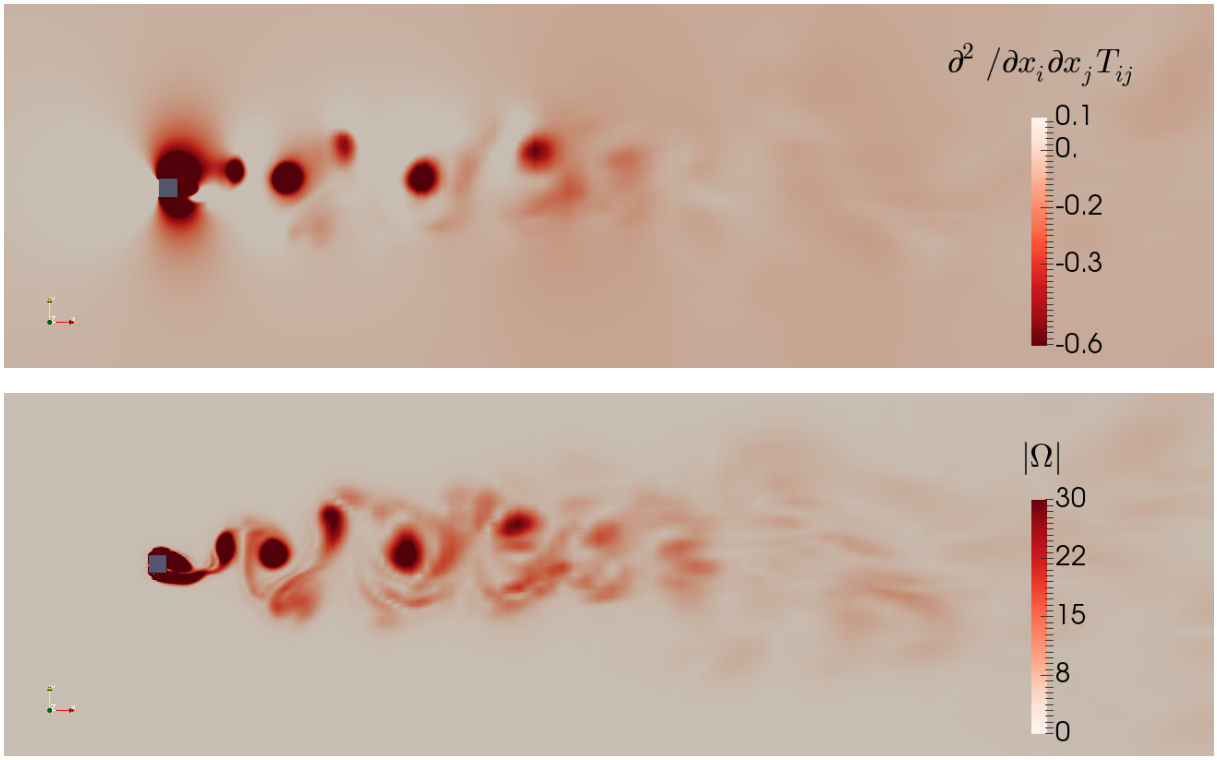

Figure 16: Contour plot of instantaneous $\dfrac{\partial^2}{\partial x_i \partial x_j} T_{ij}$ (top panel) and magnitude of the vorticity $|\Omega|$ (bottom panel).

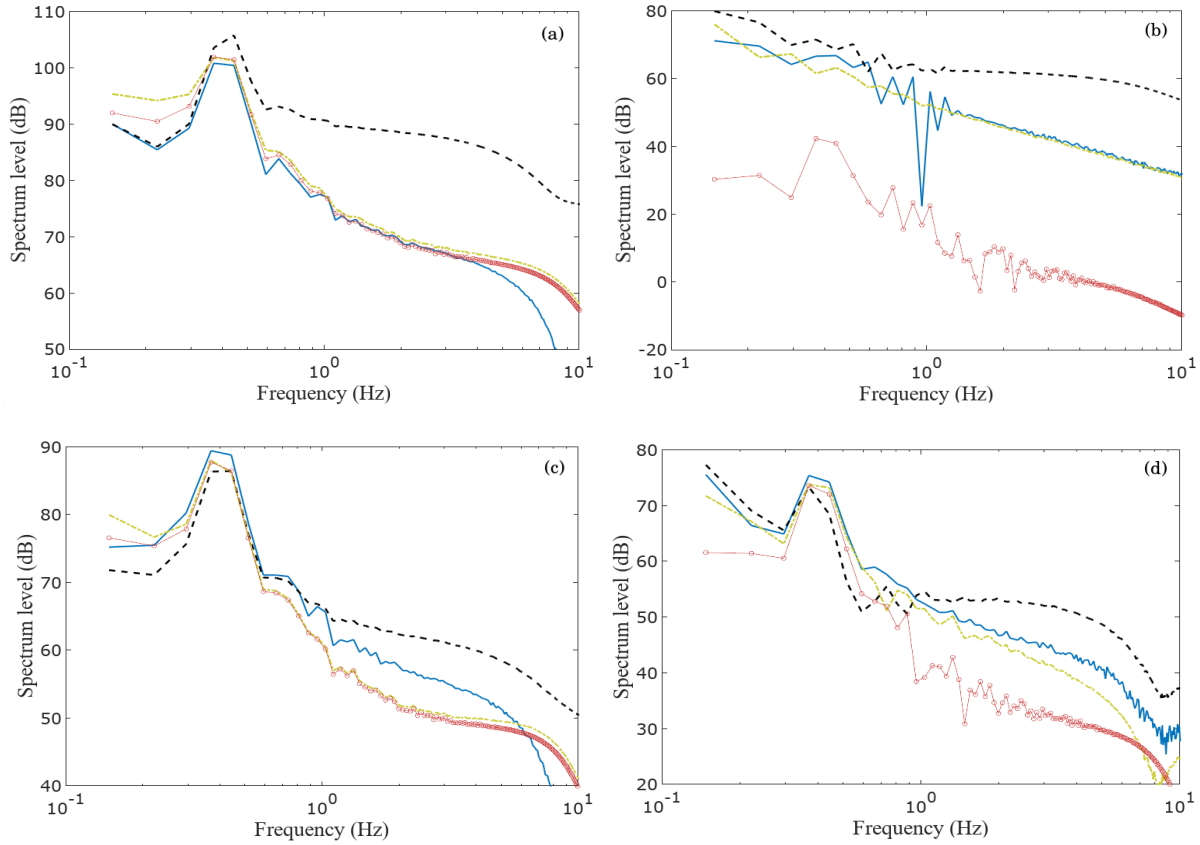

Figure 17: Pressure spectra obtained by LES (——), Curle (linear) (—o—), porous (- - - -) and direct (-·-·-) solution: Microphones M1 (a) and M2 (b) calculated with box B1; Microphones M3 (c) and M4 (c) calculated with box B2 (bottom panels). Grid G2.

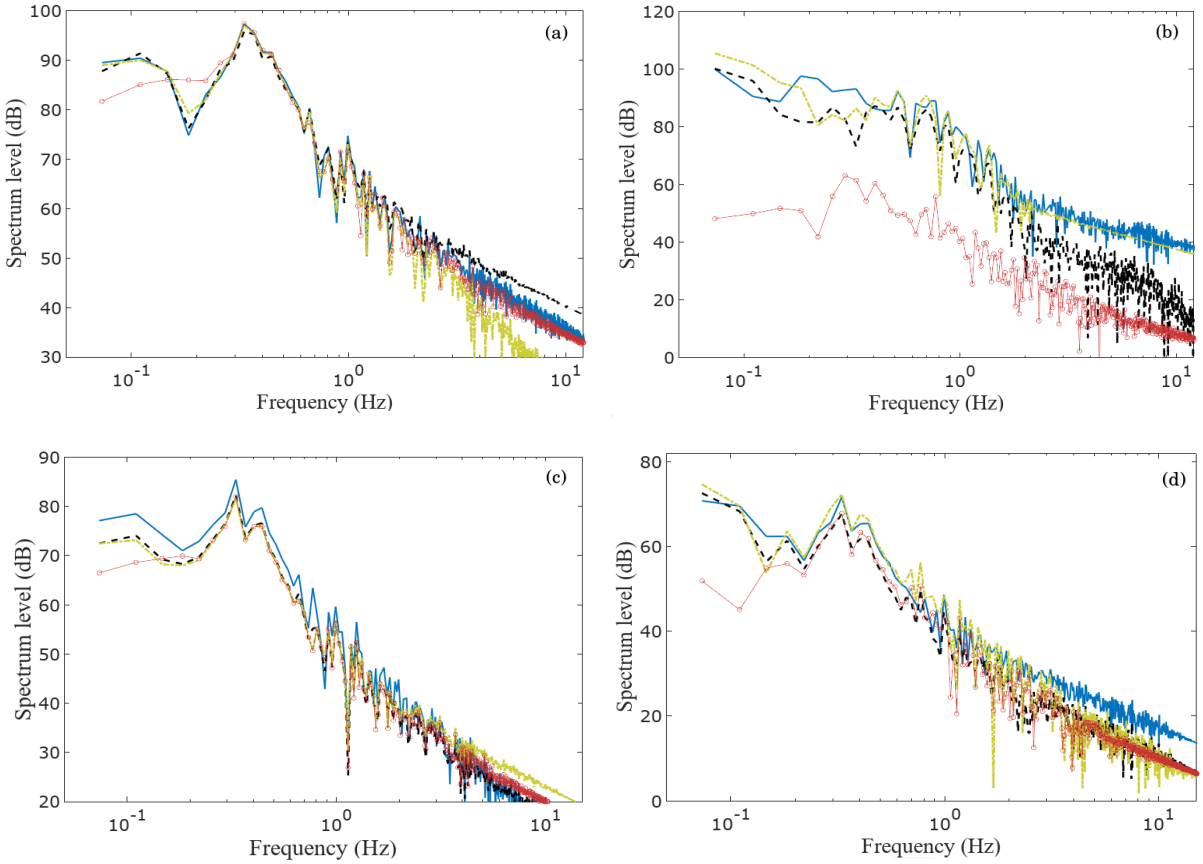

Figure 18: Pressure spectra obtained by LES (——), Curle (linear) (—o—), porous (- - - -) and direct (-·-·-) solution: Microphones M1 and M2 calculated with box B1 (top panels); Microphones M3 and M4 calculated with box B2 (bottom panels). Grid G3.

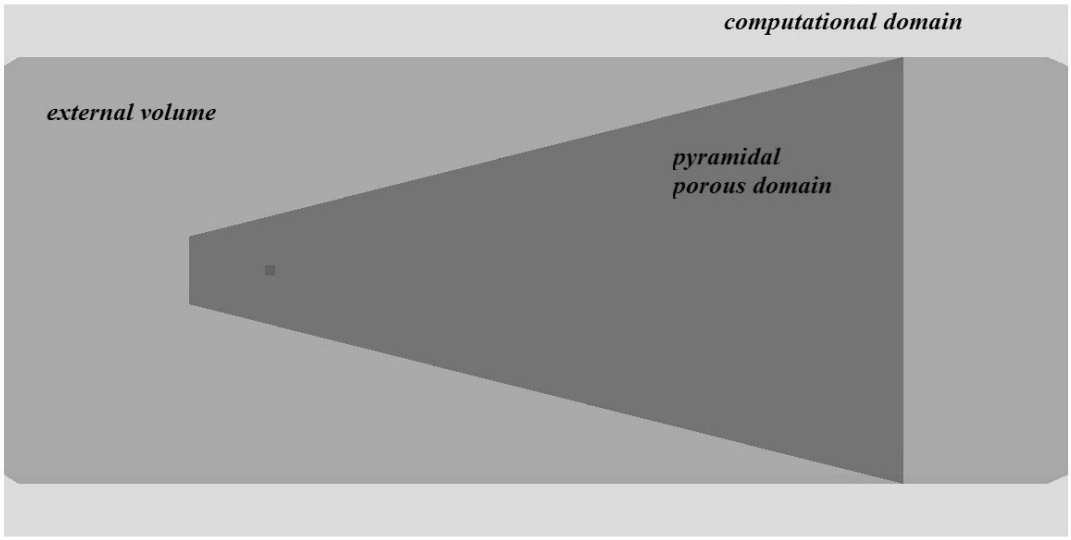

Figure 19: Sketch of the domains adopted to couple the porous and direct approaches. A pyramidal porous surface and a surrounding external volume, enclosed in the box B2 of Figure 11.

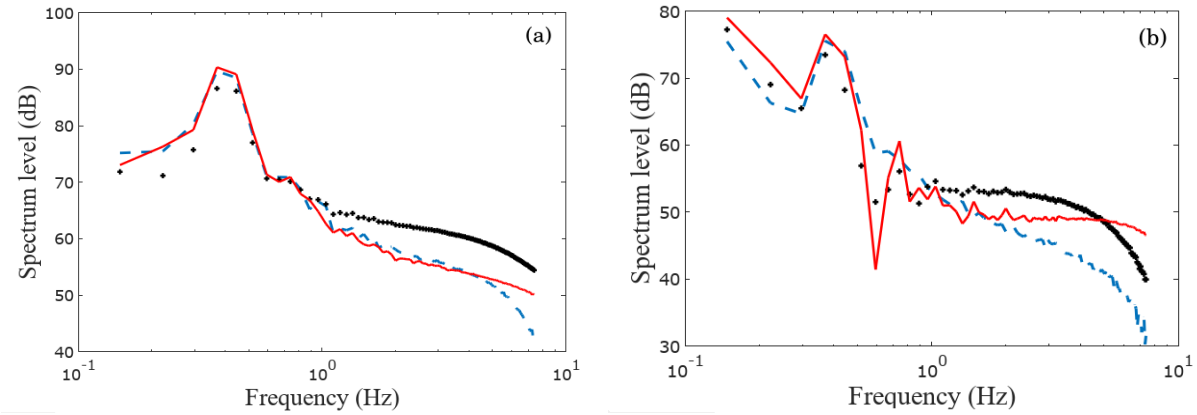

Figure 20: Pressure spectra at probes M3 (a) and M4 (b) determined by adding to the porous solution on the pyramidal surface the volume integrals computed on the external volume, as depicted in previous Figure 19. Reference pressure LES (- - - -); FW-H porous (+); complete porous (——).

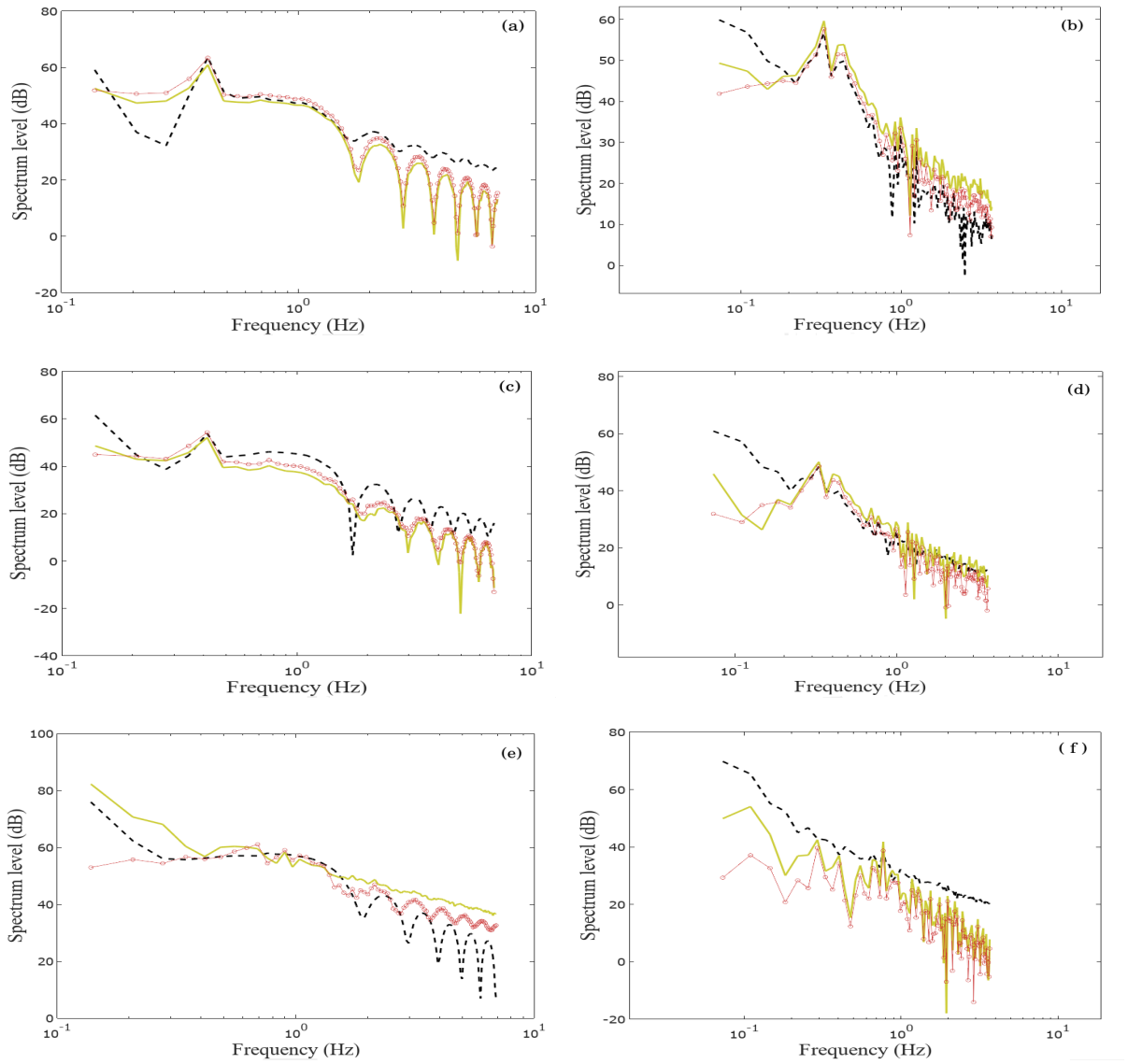

Figure 21: Acoustic far-field: comparison of FW-H linear terms (—o—), direct (——) and porous (- - - -) formulation for three michrophones M_f1 (a,b), M_f2 (c,d), and M_f3 (e,f), from top to bottom. Case G2 left panels (a,c,e) and case G3 right panels (b,d,f).